Postprint of a paper published in *Powder Technology*, 29(2016):17-33. Version of record is available at http://dx.doi.org/10.1016/j.powtec.2016.04.006

Synthesis of stoichiometrically controlled reactive aluminosilicate and calcium-aluminosilicate powders

Brant Walkley[1], Rackel San Nicolas[1, 2], Marc-Antoine Sani[3], John D. Gehman[3,4], Jannie S.J. van Deventer[1, 5], John L. Provis[6,*]

[1] *Department of Chemical and Biomolecular Engineering, The University of Melbourne, Victoria 3010, Australia*

[2] *Department of Infrastructure Engineering, The University of Melbourne, Victoria 3010, Australia*

[3] *School of Chemistry and Bio21 Institute, The University of Melbourne, Victoria 3010, Australia*

[4] *GehmanLab, Woodend, Victoria 3442, Australia*

[5] *Zeobond Pty Ltd, P.O. Box 23450, Docklands, Victoria 8012, Australia*

[6] *Department of Materials Science and Engineering, The University of Sheffield, Sheffield S1 3JD, United Kingdom*

* Corresponding author. Email: j.provis@sheffield.ac.uk, phone: +44 114 222 5490

Abstract

Aluminosilicate and calcium-aluminosilicate powders are synthesised via an organic steric entrapment route under conditions permitting strict stoichiometric control, utilising polyvinyl alcohol and polyethylene glycol as polymeric carriers. Polyethylene glycol is superior to polyvinyl alcohol for synthesis of calcium-aluminosilicate powders via this method, producing a more controllable product which generated less fine ash during calcination. This paper presents detailed description of synthesis and characterisation of the powders produced through this approach, including new insight into the nanostructures within the calcined powders. Aluminium environments are a mixture of 4-, 5- and 6-coordinated, while silicon is tetrahedral and shows a broad range of connectivity states. The powders are X-ray amorphous, display a high degree of homogeneity, and thus offer potential for utilisation as precursors for synthesis of hydrous aluminosilicates in the quaternary $CaO–Na_2O–Al_2O_3–SiO_2$ system.

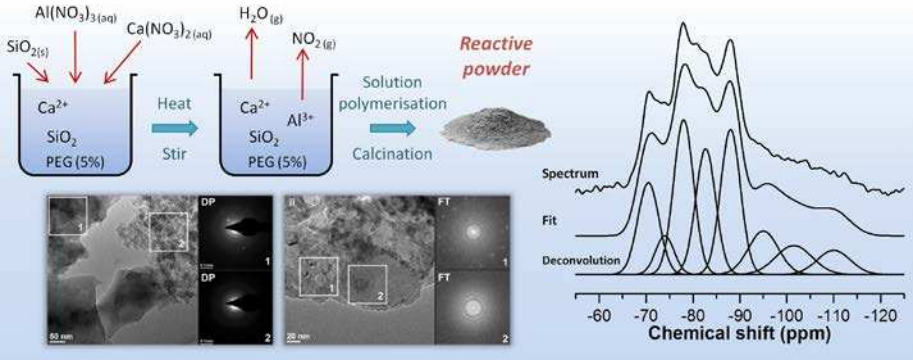

Keywords: amorphous aluminosilicates, powder synthesis, NMR spectroscopy

Postprint of a paper published in *Powder Technology*, 29(2016):17-33. Version of record is available at http://dx.doi.org/10.1016/j.powtec.2016.04.006

1. Introduction

In recent years, the production of ceramic powders via chemical synthesis routes has gained significant attention in academia and industry as a method of increasing energy efficiency when compared with production by traditional high-temperature solid-state reactions, as well as offering scope for production of chemical or phase compositions which are difficult to achieve via solid state routes. The Pechini process [1], for example, is a solution-polymerisation route which allows the production of homogeneous single phase mixed oxide powders by the use of an organic acid to chelate metal ions, and has been key to the development of ceramic synthesis via chemical routes.

A number of studies have used variations of the Pechini process to synthesise calcium, silicon or aluminium-containing mixed oxides by employing an organic polymeric steric entrapment solution-polymerisation route [2-6]. This method utilises a long chain organic polymer, most commonly polyvinyl alcohol (PVA), to sterically inhibit the movement of the metal cations during solution polymerisation, forming a homogeneous single phase mixed oxide powder upon drying and moderate-temperature calcination to remove the organic component [2, 5, 7]. Of the studies utilising the organic polymeric steric entrapment solution-polymerisation route, most focus on the synthesis of mixed oxides for ceramic applications [2-4, 6], others describe synthesis of an apparently 'metakaolin-like' powder which can be subsequently activated to form a geopolymeric binder [8, 9], while one study described the use of this route to individually synthesise each of the reactive phases which are present in Portland cement (PC) [5].

Geopolymers, or alkali-activated binders, are produced by chemical reaction of an aluminosilicate or calcium-aluminosilicate powder with an alkaline solution to form a solid binder with properties comparable to those of hardened PC [10, 11]. These materials offer a viable environmentally friendly replacement for PC, with a reduction in the associated CO_2 emissions of between 50% and 80% when compared to PC binders [12]. Furthermore, as the raw materials used to produce geopolymers are often industrial by-products such as blast furnace slag and fly ash, or readily available aluminosilicate clay-based products such as metakaolin (calcined kaolinite), they present an avenue for the use of, and add value to, these materials.

Geopolymer formulations must be carefully designed to obtain desirable rheological, chemical and physical properties, and this can only be achieved through a detailed understanding of complex particle interactions occurring within the packed geopolymer mortar and concrete systems [13-16]. This can be particularly challenging due to the wide variation of chemical and physical characteristics exhibited by commercial geopolymer precursors where a range of chemical reactivity is observed,

meaning it is often difficult to distinguish reactive from inert species. This is further complicated by the introduction of alkali-reactive aggregates in geopolymer concrete systems [17, 18].

A large number of studies are focused on understanding the chemistry of geopolymers and alkali-activated binders, however the literature is often conflicting and experimental analysis involves a large number of unconstrained parameters. To gain insight into the effect of precursor chemical composition on the chemical and physical interactions occurring within the complex particulate system formed during geopolymer synthesis, a method of studying geopolymers which permits strict stoichiometric control must be developed. This, in turn, can only be achieved through synthesis of aluminosilicate and calcium-aluminosilicate powders via a route through which strict control of the chemistry is obtained.

The present study applies the knowledge gained through development of the aforementioned chemical synthesis routes for ceramic powder production. Specifically, the organic polymeric steric entrapment solution-polymerisation route is refined and adjusted, including the use of PEG rather than PVA for calcium-containing systems, to develop a novel class of laboratory synthesised, stoichiometrically controlled reactive high-purity geopolymer precursor powders.

2. Experimental

2.1 Powder synthesis

2.1.1 Aluminosilicates

A 5 wt.% polyvinyl alcohol (PVA) solution was made by adding 98-99% hydrolysed PVA (Sigma Aldrich, molecular weight 31 - 50 kDa) to distilled water. PVA of this molecular weight has been shown to produce more reactive calcium silicate and calcium aluminate powders with higher specific surface areas, compared to longer-chain PVA [5]. The polymer was added to distilled water in small increments over heat and the resulting solution was stirred at 60 ^{o}C for 1 hour. Aluminium nitrate nonahydrate, $Al(NO_3)_3{\cdot}9H_2O$ (Sigma Aldrich 98.5 wt. %) was added to distilled water to produce a 40 wt.% solution, which was then added to the 5 wt. % PVA solution and stirred at 60 ^{o}C for one hour before addition of colloidal silica (Sigma Aldrich Ludox HS-40 colloidal silica (SiO_2), 40 wt. % in water). The stoichiometry was designed to achieve the elemental ratios outlined in Table 1, as well as ensuring that the number of metal cations (M^{x+}) in solution was significantly more than the number that the PVA could chemically bind through its OH groups (M^{x+}/OH = 4) [2, 5]. Water was evaporated from the resulting solution by stirring over heat at 80 ^{o}C, to form a viscous aerated gel. A portion of each aerated gel was

kept for analysis by differential thermogravimetric analysis (DTG), while the remaining dry aerated gel was calcined by heating at 3 °C/min to 550 °C in a laboratory muffle furnace, with a 1 hour hold time at 550 °C and then cooling in air, to produce a fine white powder which was subsequently ground by hand before characterisation.

Table 1: Molar ratios, polymer carrier and metal valence (M^{x+}) to hydroxyl functionality (OH) ratio for each sample

Sample	Empirical formula	Ca/(Al+Si)	Al/Si	Polymer	M^{x+}/OH
A	$2SiO_2 \cdot Al_2O_3$	0.000	1.000	PVA	4
B	$4SiO_2 \cdot Al_2O_3$	0.000	0.500	PVA	4
C	$0.800CaO \cdot SiO_2 \cdot 0.078Al_2O_3$	0.692	0.156	PEG	2
D	$1.214CaO \cdot SiO_2 \cdot 0.078Al_2O_3$	1.050	0.156	PEG	2
E	$0.709CaO \cdot SiO_2 \cdot 0.026Al_2O_3$	0.675	0.051	PEG	2
F	$1.104CaO \cdot SiO_2 \cdot 0.026Al_2O_3$	1.050	0.051	PEG	2

2.1.2 Calcium-aluminosilicates

A 5 wt. % polyethylene glycol (PEG) solution was produced by adding PEG (Sigma Aldrich, MW 20 kDa) to distilled water. The requirement for the use of PEG instead of PVA is due to the presence of the calcium, and will be discussed in more detail below (section 2.2). The polymer was added to distilled water in small increments over heat, and the resultant solution was stirred at 60 °C for 1 hour. Aluminium nitrate nonahydrate, $Al(NO_3)_3 \cdot 9H_2O$ (Sigma Aldrich, 98.5 wt. %) and calcium nitrate tetrahydrate, $Ca(NO_3)_2 \cdot 4H_2O$ (BDH Prolabo, VRW International, 99.0 wt. %) were each added to distilled water to produce 40 wt.% solutions by mass of anhydrous salt, and these solutions were subsequently added to the 5 wt. % PEG solution and stirred at 60 °C for one hour before addition of colloidal silica (Sigma Aldrich Ludox HS-40 colloidal silica (SiO_2), 40 wt.% in water). As in the aluminosilicate powder synthesis, the stoichiometry was designed to achieve the elemental ratios outlined in Table 1, as well as ensuring that the number of metal cations (M^{x+}) in solution was significantly more than the number that PEG polymer carrier could chemically bind through its OH groups (M^{x+}/OH = 2). Water was evaporated from the resulting solution by stirring over heat at 80 °C to form a viscous aerated gel which was then placed in a drying oven at 100 °C overnight to remove any remaining water. A portion of each aerated gel was kept for analysis by differential thermogravimetric analysis (DTG), while the remaining dry aerated gel was calcined at 3 °C/min to 900

Postprint of a paper published in *Powder Technology*, 29(2016):17-33. Version of record is available at http://dx.doi.org/10.1016/j.powtec.2016.04.006

°C in a laboratory muffle furnace, with a 1 hour hold time at 900 °C and then cooling in air, producing a fine white powder which was subsequently ground by hand before characterisation.

The stoichiometric ratios for these samples were chosen to provide a chemically simplified model system for aluminosilicate and calcium-aluminosilicate alkali-activated binder precursors. Samples A and B (empirical formulas $2SiO_2{\cdot}Al_2O_3$ and $4SiO_2{\cdot}Al_2O_3$, respectively) were chosen to represent the range of bulk silicon and aluminium content typically found in fly ashes, with A also representing the approximate composition of metakaolin (see Figure 1) [19]. Samples C, D, E and F (empirical formulas $0.800CaO{\cdot}SiO_2{\cdot}0.078Al_2O_3$, $1.214CaO{\cdot}SiO_2{\cdot}0.078Al_2O_3$, $0.709CaO{\cdot}SiO_2{\cdot}0.026Al_2O_3$ and $1.104CaO{\cdot}SiO_2{\cdot}0.026Al_2O_3$, respectively) were chosen to enable synthesis of binders exhibiting chemistry in regions of the quaternary $CaO - Na_2O - Al_2O_3 - SiO_2$ system which are important for the study of sodium- and aluminium-substituted calcium silicate hydrate gels, the main reaction product present in alkali-activated slag binders [11, 20].

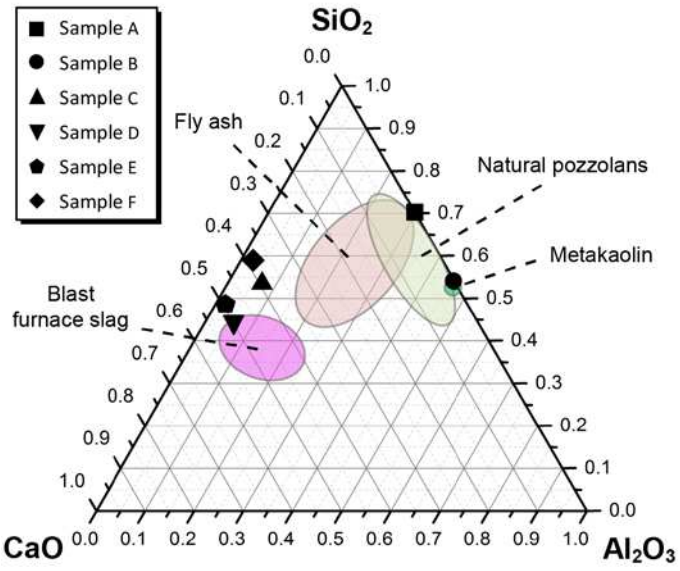

Figure 1: Projection of powder chemistry onto the ternary Ca – Al – Si system showing elemental composition (mass basis) of each powder, as well as the compositional range for common supplementary cementitious materials based on [21]

2.2 Practical considerations

An organic steric entrapment solution-polymerisation route utilising PVA has been previously reported to enable synthesis of a range of cementitious phases including dicalcium silicate, tricalcium silicate, tricalcium aluminate and tetracalcium aluminoferrite, as well as other mixed oxides [2-6],

however we observed polyvinyl alcohol to be unsuitable as a polymer carrier in the synthesis of calcium-aluminosilicate powders. In the calcium-free systems A and B here, calcination of the precursor at 550°C to remove PVA yielded fine white powders with greater than 96 wt.% yield. However, when PVA was used as the polymer carrier for synthesis of calcium-aluminosilicate powders, calcination at 550°C resulted instead in the formation of a very fine ash which could not be recovered. The calcination temperature for the calcium-aluminosilicate powders was increased to 900 °C to avoid formation of $CaCO_3$ or charring of PVA, but this was unsuccessful, and unrecoverable fine ash was again produced. Replacing PVA with PEG as the polymer carrier, it became possible to calcine the calcium-aluminosilicate powders for complete removal of the polymer carrier, producing a highly reactive, predominantly amorphous product. It was important to take significant care to maintain the temperature at 80 °C during evaporation of water from the aerated PEG gels, to avoid rapid combustion and charring of the PEG polymer. This was achieved by measuring temperature using a standard laboratory thermometer and adjusting the amount of heat provided by the hotplate as required. Calcination of all of the samples produced a fine white powder, homogeneous and with no visible residual carbon. To elucidate the chemical and physical interactions occurring between the polymer and ceramic powder the aluminosilicate powders were also synthesised utilising PEG as the polymer carrier, using the same method as outlined in section 2.1.2.

2.3 Characterisation

Chemical composition data were obtained by energy dispersive X-ray Fluorescence (XRF) spectrometry using a Spectro 'Xepos' instrument. Sample preparation involved fusion with a 12:22 lithium tetraborate:metaborate flux in platinum crucibles at 1050°C for 15 minutes to produce a glass bead.

The Brunauer-Emmett-Teller (BET) surface area [22] of each powder was determined by nitrogen sorption on a Micromeritics (Norcross, GA) ASAP2010 instrument. Barrett-Joyner-Halenda (BJH) desorption pore size and volume analysis [23] were applied to determine the pore size distribution of the mesopores, while the Horvath-Kawazoe method [24] with Saito-Foley modification [25] was applied to determine the micropore distribution, with interaction parameters for N_2 adsorbate taken from [24] and aluminosilicate adsorbent from [25].

The particle size distribution of the powders was determined using a Malvern Mastersizer 2000 laser diffraction particle size analyser employing ultrasonic dispersion and assuming a refractive index of 1.53 for aluminosilicate powders and 1.62 for calcium-aluminosilicate powders [26, 27]. Samples were ground by hand using a mortar and pestle.

Differential thermogravimetric (DTG) analysis was performed on powdered samples of approximately 30 mg in an alumina crucible using a Perkin Elmer Diamond instrument, at a heating rate of 10 ^{o}C/min between 30 ^{o}C and 1000 ^{o}C with a nitrogen purge at 200 mL/min for aluminosilicate powders, and a heating rate of 3 ^{o}C/min between 30 ^{o}C and 1000 ^{o}C in ambient air for calcium-aluminosilicate powders. To ensure consistency between the initial states of each sample, the samples were held in the instrument at 30°C for 20 minutes prior to the commencement of heating.

Combined differential thermogravimetric-mass spectrometry (DTG-MS) analysis was performed using a Perkin Elmer TGA4000 coupled to a Hiden Analytical Mass Spectrometer for gas analysis, at a heating rate of 10 ^{o}C/min between 30 ^{o}C and 1000 ^{o}C in ambient air for aluminosilicate precursors and a heating rate of 3 ^{o}C/min between 30 ^{o}C and 1000 ^{o}C in ambient air for calcium-aluminosilicate precursors. To ensure consistency between the initial states of each sample, the samples were held in the instrument at 30°C for 20 minutes prior to the commencement of heating. Nitrogen, oxygen, water vapour, carbon monoxide, carbon dioxide, methane and hydrogen were analysed. Deconvolution of the mass spectrometry data was performed using industry standard relative sensitivities and fragment ratios.

X-ray diffraction (XRD) experiments were performed using a Bruker D8 Advance instrument with Ni-filtered Cu Kα radiation, a step size of 0.020^{o}, dwell time of 3 seconds and a 2θ range of 3 - 70^{o}.

Solid state ^{29}Si MAS NMR spectra were collected at 119.141 MHz on an Agilent (Varian) VNMRS-600 (14.1 T) spectrometer using a probe for 4 mm outer diameter zirconia rotors and a spinning speed of 10.0 kHz. The ^{29}Si MAS NMR experiments for aluminosilicate powders (samples A and B) employed a pulse width of 4 µs, a pulse angle of 47^{o}, a relaxation delay of 45 s, and 1024 scans, while ^{29}Si MAS NMR experiments for calcium-aluminosilicate powders (samples C, D, E and F) employed a pulse width of 7 µs, a pulse angle of 90^{o}, a relaxation delay of 120 s, and 1024 scans. Solid state ^{27}Al MAS NMR spectra were acquired on the same instrument at 156.261 MHz and a spinning speed of 10.0 kHz, with a pulse width of 4 µs, a pulse angle of 90^{o}, a relaxation delay of 2 s and 1024 scans. ^{29}Si and ^{27}Al chemical shifts were referenced to external samples of tetramethylsilane (TMS) and aluminium chloride hexahydrate, $AlCl_3 \cdot 6H_2O$, as a 1.0 M aqueous solution or as a powder, for aluminosilicate powders and calcium-aluminosilicate powders respectively, at 0 ppm. All data were processed using NMRPipe [28]. Deconvolution of the ^{29}Si MAS NMR spectra was performed using Gaussian peak profiles [29]. A single Gaussian peak was used to represent each expected $Q^n(m\text{Al})$ species, and these peaks were used to develop a simulation of the ^{29}Si MAS NMR spectra using a least squares fitting method. Peak assignments were made with reference to the literature, and references are provided in the main text. The minimum possible number of peaks was used to enable an accurate and

Postprint of a paper published in *Powder Technology*, 29(2016):17-33. Version of record is available at http://dx.doi.org/10.1016/j.powtec.2016.04.006

meaningful interpretation of the spectra, with the requirement that the intensities of adjacent peaks vary smoothly, consistent with the thermodynamics of a statistical distribution of Si and Al sites within an aluminosilicate network [30, 31].

Transmission electron microscopy (TEM) was performed using an FEI Tecnai F20 instrument fitted with an Apollo Silicon Drift Detector (EDAX instruments) for energy dispersive X-ray analysis and a spot size of 100nm. Samples were ground by hand in isopropyl alcohol (IPA) using a mortar and pestle. The fines were separated by ultrasonic dispersion and density separation, followed by removal of the top layer of fluid with a pipette. A single drop of IPA containing the fine particle dispersion was placed onto holey carbon film on a 300 µm mesh Cu grid (Agar Scientific) and allowed to dry before analysis.

3. Results and Discussion

3.1 Chemical and physical characterisation of powders

The bulk oxide composition of each powder formulation as determined by X-ray fluorescence analysis is presented in Table 2. Each powder is measured to be within 1 wt. % of its target composition, which is approximately the expected uncertainty associated with the XRF measurements. The BET surface areas (determined from N_2 adsorption isotherms, Figure 2) and the D_{50} particle size as determined by laser diffraction analysis of the calcined powder for each sample are given in Table 3.

Table 2: Bulk oxide composition of each powder formulation as determined by X-ray fluorescence analysis. An error of approximately 1 wt % is expected.

	Mol % (target)			***Mol % (measured)***		
Sample	CaO	SiO_2	Al_2O_3	CaO	SiO_2	Al_2O_3
A	0.0	66.7	33.3	0.0	66.4	33.6
B	0.0	80.0	20.0	0.0	79.1	20.9
C	41.6	53.2	4.2	42.1	53.8	4.1
D	53.0	43.6	3.4	53.2	43.3	3.4
E	40.1	57.6	1.5	40.3	58.2	1.5
F	51.8	47.0	1.2	51.9	46.8	1.3

Postprint of a paper published in *Powder Technology*, 29(2016):17-33. Version of record is available at http://dx.doi.org/10.1016/j.powtec.2016.04.006

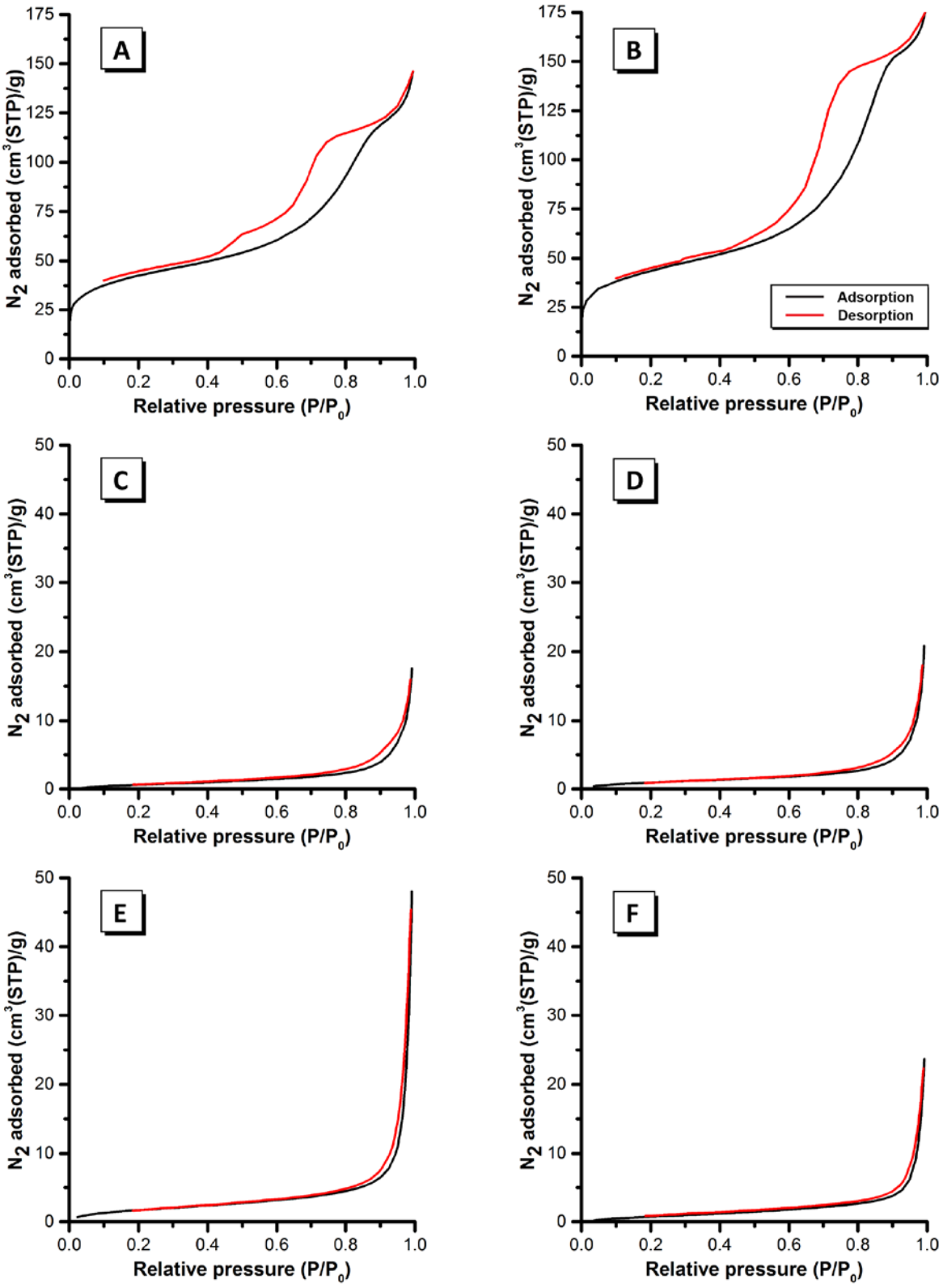

Figure 2: N_2 adsorption (black) and desorption (red) isotherms for each sample (A-F as marked)

Postprint of a paper published in *Powder Technology*, 29(2016):17-33. Version of record is available at http://dx.doi.org/10.1016/j.powtec.2016.04.006

Table 3: Brunauer-Emmet-Teller surface area and D_{50} of each calcined powder

	A	B	C	D	E	F
Surface area (m^2/g)	142	147	2.9	3.8	6.4	3.6
D_{50} (μm)	10.6	12.8	23.7	40.1	31.1	36.7

The surface areas measured for the aluminosilicate powders are an order of magnitude higher than those typically found for fly ash, which are on the order of 0.1 - 10 m^2/g [32-34]. The pore size distribution as determined by Barrett-Joyner-Halenda (BJH) desorption pore size and volume analysis (for mesopores) and by the Horvath-Kawazoe method with Saito-Foley modification (for micropores) showed three distinct pore sizes of approximately 1 nm, 4 nm and 7 nm (Figure 3). These pores are likely due to removal of the organic component from the powder during calcination, and are responsible for the high surface area. It is likely that any unburnt carbon present within the powders as a result of partial pyrolysis of the polymers will contribute significantly to the surface area and may also be a factor here.

The surface areas measured for the calcium-aluminosilicate powders an order of magnitude higher than those typically observed for ground granulated blast furnace slag (typically 0.2 - 0.8 m^2/g) [11, 35], while the pore size distribution data for all calcium-aluminosilicate powders indicate a distribution of pore sizes centred at approximately 60 - 70 nm for low-Ca samples C and E, and 20 - 50 nm for high-Ca samples D and F.

Calcination temperature will also control the surface area of ceramic oxide particles, with increasing temperature causing a decrease in particle surface area due to increased particle growth. The difference in calcination temperatures between the aluminosilicate (samples A and B) and calcium aluminosilicate powders (samples C-F) will then also contribute to the large difference in surfaces areas.

Postprint of a paper published in *Powder Technology*, 29(2016):17-33. Version of record is available at http://dx.doi.org/10.1016/j.powtec.2016.04.006

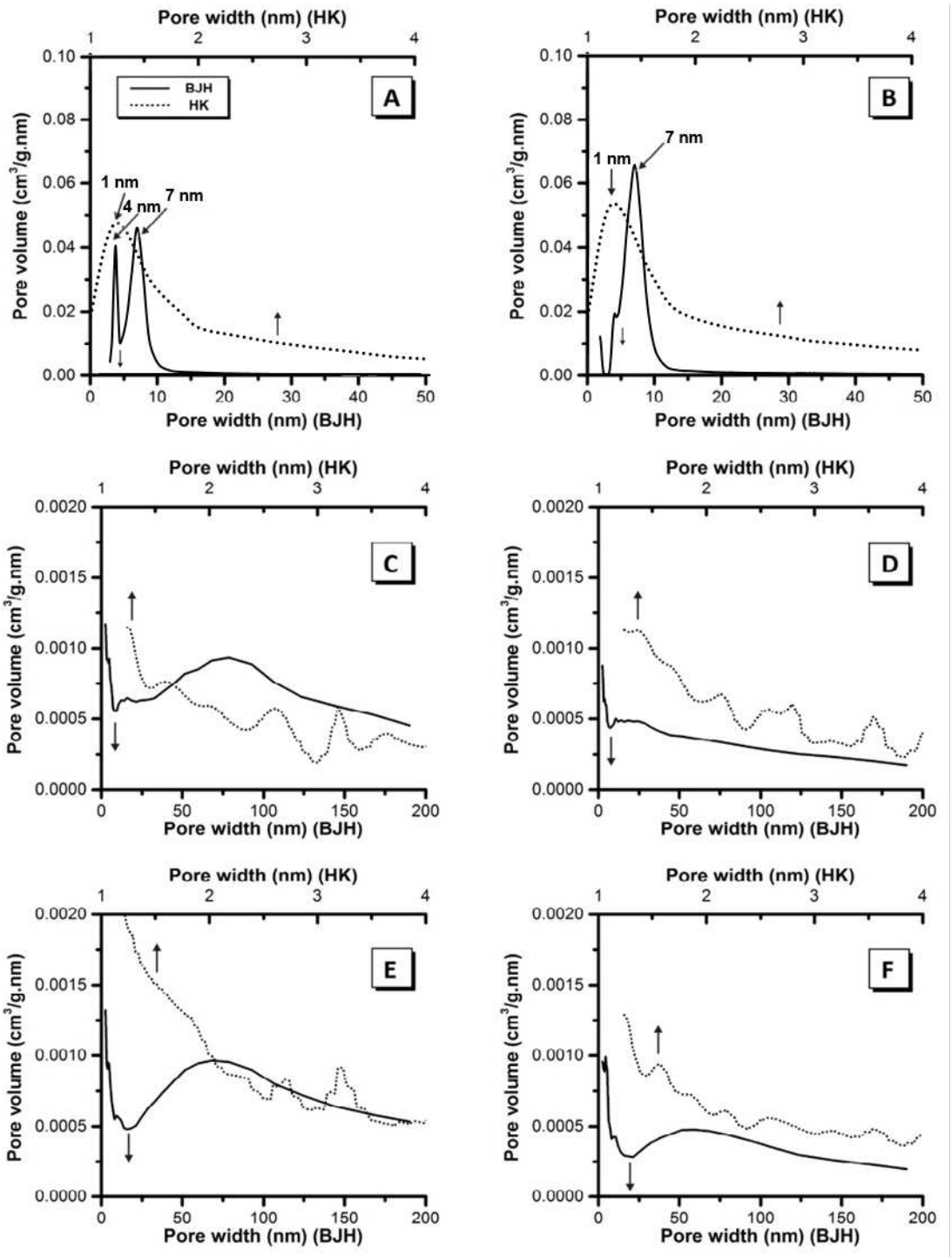

Figure 3: Pore size distribution curves for each sample A-F as marked determined using Barrett-Joyner-Halenda (BJH) desorption pore size and volume analysis [23] for mesopores (solid lines) and the Horvath-Kawazoe method [24] with Saito-Foley modification [25] for micropores (dashed lines). Interaction parameters for N_2 adsorbate taken from [24] and aluminosilicate adsorbent from [25]. Filled black arrows indicate the relevant axis for each curve.

3.2 Combined differential thermogravimetry – mass spectrometry

Postprint of a paper published in *Powder Technology*, 29(2016):17-33. Version of record is available at http://dx.doi.org/10.1016/j.powtec.2016.04.006

Differential thermogravimetric (DTG) data for the uncalcined precursors and calcined powders, as well as pure polyethylene glycol and pure polyvinyl alcohol, are presented in Figure 4 while combined DTG-MS curves for the uncalcined precursor in each sample are presented in Figure 5. The DTG curve for pure polyethylene glycol shows a single sharp peak at approximately 250°C, while that of pure polyvinyl alcohol shows two broad mass loss peaks at 275°C and 425°C and a sharp mass loss peak at 515°C.

For the uncalcined aluminosilicate precursors synthesised using PVA as the polymer carrier (samples A and B) mass loss takes place predominantly below 550 °C. The DTG curves of both samples obtained during combined DTG-MS experiments exhibit small mass loss peaks at 100 - 200 °C (coinciding with an increase in concentration of H_2O gas) and a larger mass loss peak between 250 – 400 °C (centred at approximately 330 – 340 °C) (coinciding with an increase in concentration of CO and CO_2 gas and a decrease in concentration of O_2). An increase in concentration indicates production of these gases during each respective mass loss peak. The mass loss and gas evolution profiles for samples A and B are consistent with the loss of unbound (evaporable) water and adsorbed water present as condensed hydroxyl groups on the surface of the polymeric precursor (occurring between 100 – 200 °C) and dehydroxylation and pyrolysis of the PVA polymer (occurring between 250 – 400 °C) [30, 36, 37]. No significant changes in mass are observed above 550 °C, indicating that this calcination temperature is sufficient for complete removal of the organic phases present in the polymeric precursor.

Mass loss peaks observed at approximately 100 – 200 °C in the DTG data for the calcined powders for sample A and B are attributed to the loss of the small amount of adsorbed water which has been taken up from the ambient air. The sharp mass loss peak at 250 – 350 °C seen in the DTG curves of the uncalcined precursors is not present in the DTG curves of calcined powders for samples A and B, indicating the complete removal of PVA from the aluminosilicate powder by calcination.

DTG curves for the uncalcined precursor for samples A and B synthesised using PEG as the polymer carrier (Figure 5i and j) each display mass loss peaks at 127 °C (coinciding with an increase in concentration of H_2O gas) and 345 – 352 °C (coinciding with an increase in concentration of CO, CO_2 and H_2O gas as well as a decrease in concentration of O_2) which are attributed to the removal of adsorbed and evaporable water and dehydroxylation and combustion of the PEG polymer. The DTG curve for sample B synthesised using PEG as the polymer carrier obtained during DTG-MS experiments also displays a mass loss peak at 268 °C (coinciding with an increase in concentration of H_2O, CO and CO_2 gas as well as a decrease in concentration of O_2) which is attributed to early stages of PEG dehydroxylation and combustion. In all cases the mass loss peaks vary smoothly.

Postprint of a paper published in *Powder Technology*, 29(2016):17-33. Version of record is available at http://dx.doi.org/10.1016/j.powtec.2016.04.006

The DTG curves for the uncalcined calcium-aluminosilicate precursors (samples C – F) (synthesised using PEG as the polymer carrier) obtained during combined DTG-MS experiments (Figure 5c - f) each display a mass loss peak at 120 – 150 ^{o}C which coincides with an increase in concentration of H_2O gas and is attributed to the removal of evaporable and adsorbed water, consistent with the observations in the isolated DTG experiments for these samples. Each sample also displays a mass loss peak at 220 ^{o}C which coincides with an increase in concentration of H_2O, CO and CO_2 gas, as well as a decrease in concentration of O_2, and is attributed to the beginning of dehydroxylation and combustion of the PEG polymer. Samples C and E exhibit a very sharp mass loss peak at 282 ^{o}C which coincide with very intense MS peaks due to an increase in concentration of CO, CO_2, H_2O and H_2 gas, as well as a MS peak due to a decrease in concentration of O_2 which mirrors that attributed to increased CO concentration. Consequently, this mass loss peak is attributed to the rapid combustion of PEG. Examining rescaled DTG-MS plots for these samples (Figure 5g and h) it is clear that for both samples H_2O gas production occurs at a temperature 1-2 ^{o}C lower than the production of CO gas, suggesting that dehydroxylation takes place immediately before rapid combustion of the dehydroxylated polymer. The mirroring of the MS peaks attributed to CO production and O_2 consumption suggests that combustion of PEG is occurring predominantly via the reaction $2C_{(s)} + O_{2(g)} \rightarrow 2CO_{(g)}$, although the production of CO_2 suggests that the reaction $C_{(s)} + O_{2(g)} \rightarrow CO_{2(g)}$ is also occurring. Samples D and F exhibit less intense, smoother mass loss peaks at 291 ^{o}C and 285 ^{o}C, respectively, which coincide with an increase in concentration of H_2O CO and CO_2 gas and a decrease in concentration of O_2, and thus are attributed to dehydroxylation and combustion of PEG. It is interesting to note that although the peak for each of these samples is much broader and less intense than that observed in the DTG-MS plots for samples C and E, H_2O gas production in these samples also occurs at a temperature 1-2 ^{o}C lower than the production of CO gas, suggesting that the same mechanism of PEG combustion occurs in each calcium-aluminosilicate precursor. Intermediate products formed by reactions between the uncalcined precursor and components or degradation products of the PEG during combustion will give rise to mass loss peaks at different temperatures to that observed for pure PEG combustion (Figure 4h), as will residual PEG which requires additional thermal energy for combustion due to its dispersion within the ceramic powder. It is likely that both of these situations are contributing to the differing temperatures of PEG combustion between each calcium-aluminosilicate precursor and pure PEG.

The combustion of the PEG polymer in calcium-aluminosilicate precursors appears to produce a greater amount of H_2O gas than CO and CO_2 gas, suggesting that significant quantities of tightly bound water are still present within the PEG polymer until rapid combustion occurs. Conversely, dehydroxylation and removal of water from the PEG polymer in the aluminosilicate precursors (synthesised with PEG – see Figure 5i and j) occur much less rapidly and across a larger temperature

range (from 200 – 360 °C), and the main stage of PEG combustion produces significantly more CO gas than H_2O and CO_2 gas (which are produced in approximately equal amounts). The presence of calcium in the precursors appears to alter the way in which water is held, causing it to be more tightly bound and requiring greater heat input to facilitate its removal. Once sufficient heat has been supplied to facilitate dehydroxylation, water is rapidly released immediately before combustion of the remnant organics. Rapid dehydroxylation will require significant heat input, and a sudden drop in temperature may occur. This is consistent with the observation of a rapid decrease in temperature ($\Delta T = 25^oC$) during combustion of samples E and F by isolated TGA experiments (Figure 6).

Oxygen atoms are present in PVA ($[CH_2CH(OH)]_n$) solely within hydroxyl groups (one hydroxyl group per monomer), however PEG ($H[OCH_2CH_2]_nOH$) contains oxygen atoms throughout the carbon backbone, as well as in two terminal hydroxyl groups. Consequently, in calcium-aluminosilicate precursors where water is more tightly bound, during calcination PVA will undergo rapid dehydroxylation resulting in a complete loss of oxygen from the polymer backbone and leaving solid carbon (char). After PEG undergoes dehydroxylation, however, one atom of oxygen for every two atoms of carbon still remains in the polymer backbone. This, along with oxygen present in the immediate atmosphere, appears to be sufficient to enable complete combustion of carbon via the reactions discussed above. This mechanism is consistent with observations of pyrolysis of PEG (of varying molecular weights) by mass spectrometry, where at lower temperatures homolytic cleavage of C-O bonds occurs during the onset of pyrolysis, followed by homolytic cleavage of C-C bonds at higher temperatures [38, 39]. The ratio $CO_{(g)}/CO_{2(g)}$ is a strict function of the residual $O_{2(g)}$ pressure in the system, and consequently by altering this pressure it is possible to manipulate the extent of combustion.

The DTG curves for the uncalcined precursor for samples D and F (Ca/(Al+Si) = 1.214 and 1.104; Figure 5d and f) also display small mass loss peaks at 705 °C and 686 °C, respectively, which coincide with the production of CO and CO_2 gas without any alteration in the MS signal due to O_2. This peak is attributed to the decomposition of calcite (produced by the reaction of the CaO present in the precursor with CO_2 released during combustion of PEG [37]) to free lime via the reaction $CaCO_{3(s)} \rightarrow CaO + CO_{2(g)}$.

The DTG curve of the calcined powder for samples C, D, E and F is relatively flat and does not display any of the peaks observed in the DTG curves of the precursor or pure PEG, indicating that complete removal of PEG from the powder has been achieved during calcination at 900°C, as expected. Calcination has also facilitated the removal of $CaCO_3$ from the calcined powders, as indicated by the absence of the peak at 680°C from the DTG curves of the calcined powder for these samples. The

relative amount of polymer retained by the solid in each sample (before calcination) is calculated from the TG curves (Figure 6) and detailed in Table 4.

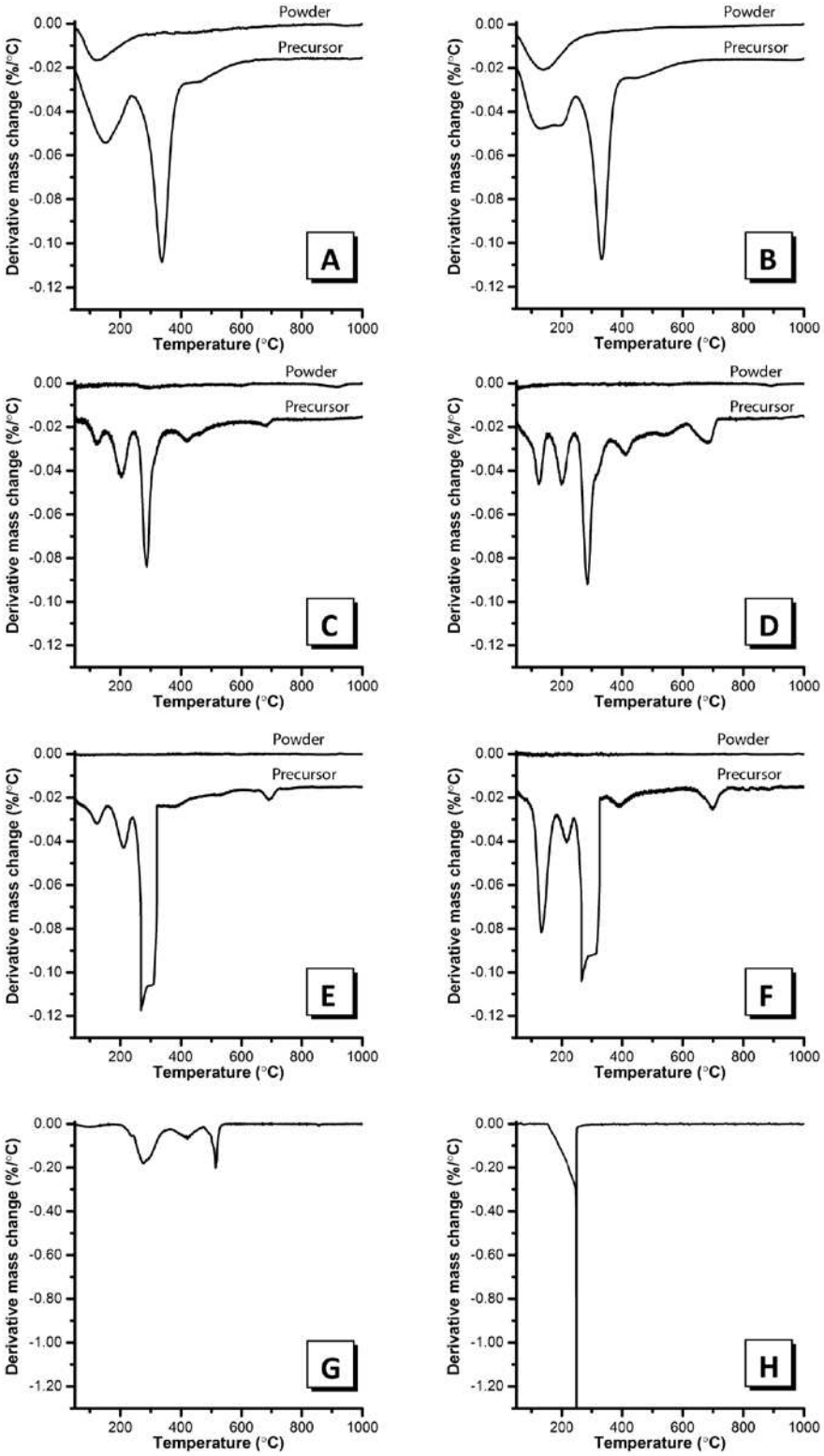

Figure 4: Differential thermogravimetric curves of the uncalcined precursor and calcined powder for: (A-F) samples A-F as marked, G) pure polyvinyl alcohol powder and H) pure polyethylene glycol powder. Successive curves are offset by 0.015 units for clarity.

Postprint of a paper published in *Powder Technology*, 29(2016):17-33. Version of record is available at http://dx.doi.org/10.1016/j.powtec.2016.04.006

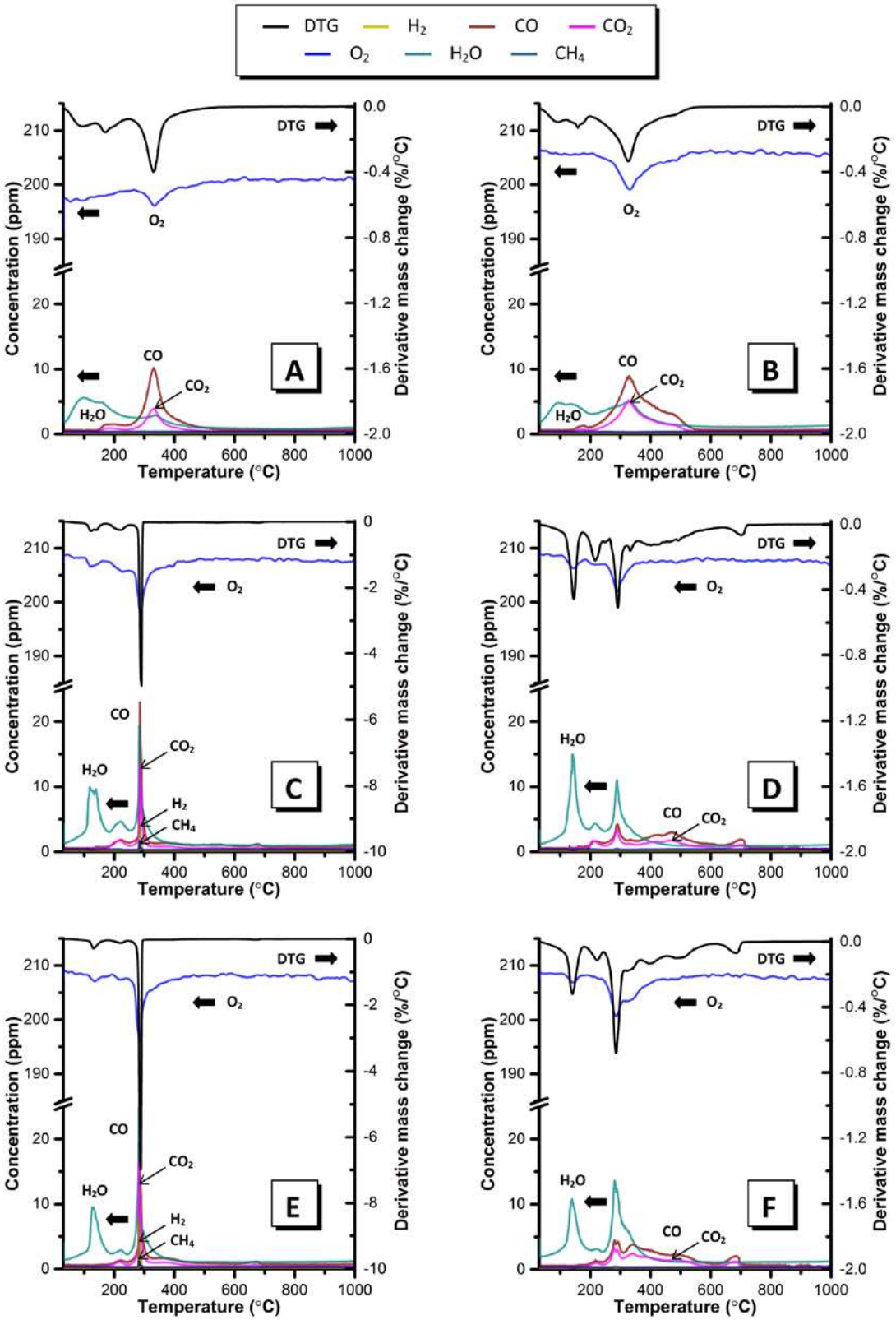

Postprint of a paper published in *Powder Technology*, 29(2016):17-33. Version of record is available at http://dx.doi.org/10.1016/j.powtec.2016.04.006

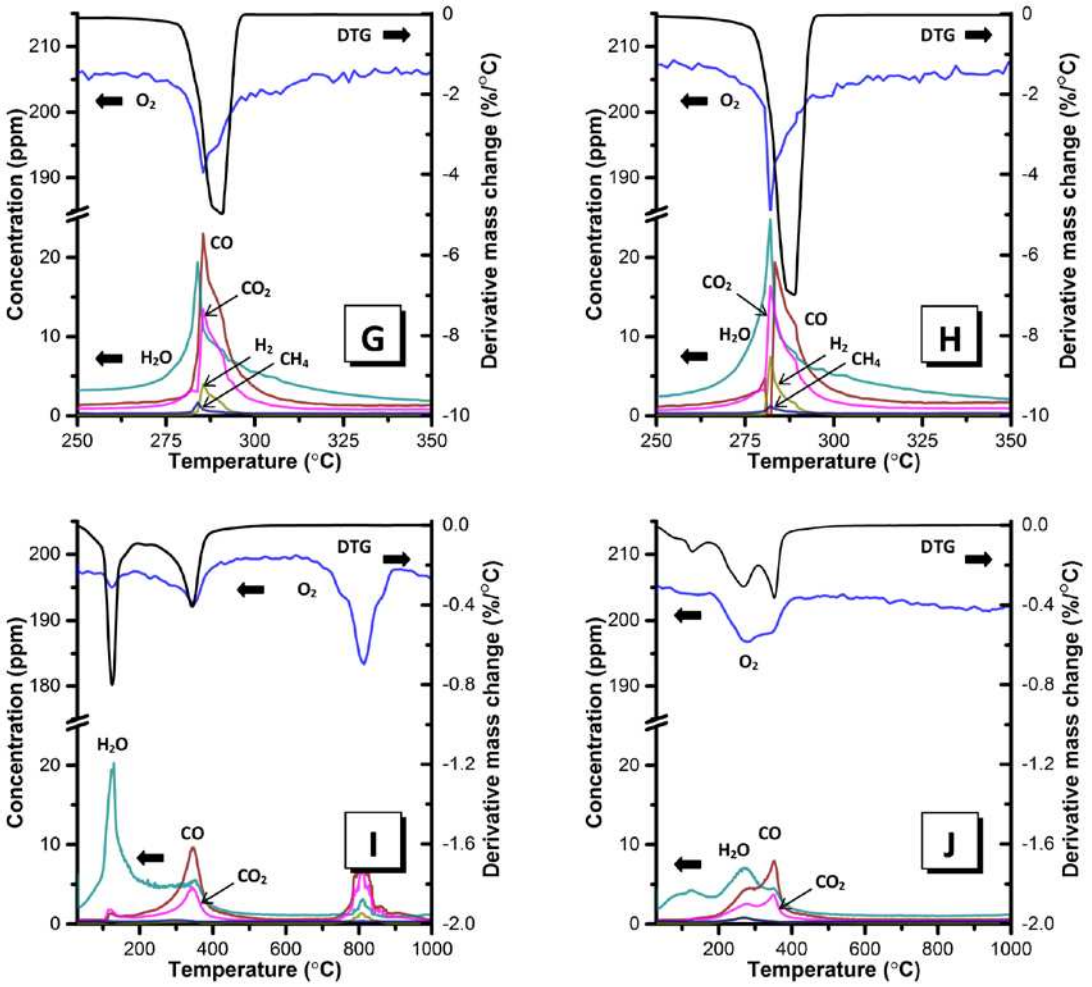

Figure 5: Combined differential thermogravimetric-mass spectrometry curves of the uncalcined precursor for: (A-F) samples A-F as marked, G) rescaled plot for sample C, H) rescaled plot for sample E, I) $2SiO_2.Al_2O_3$ synthesised using PEG as the polymer carrier and J) $4SiO_2.Al_2O_3$ synthesised using PEG as the polymer carrier. Filled black arrows indicate relevant axis for each curve.

Table 4: Relative total mass loss during calcination for each sample

Sample	**A**	**B**	**D**	**D**	**E**	**F**
Polymer	PVA	PVA	PEG	PEG	PEG	PEG
Mass loss (%)	49.1	39.4	63.0	65.0	63.8	69.2

Postprint of a paper published in *Powder Technology*, 29(2016):17-33. Version of record is available at http://dx.doi.org/10.1016/j.powtec.2016.04.006

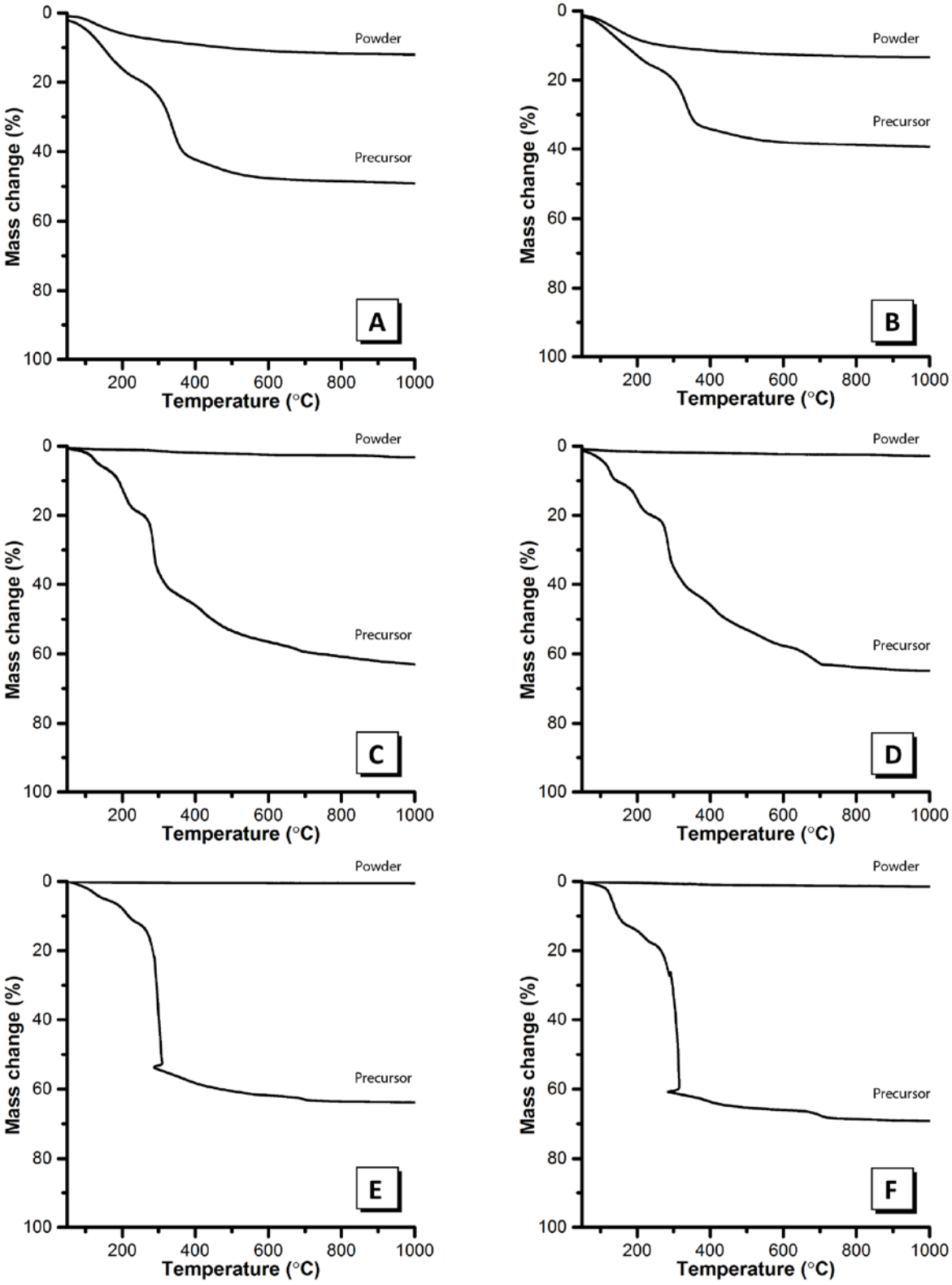

Figure 6: Thermogravimetric curves of the uncalcined precursor and calcined powder for samples A-F as marked.

Postprint of a paper published in *Powder Technology*, 29(2016):17-33. Version of record is available at http://dx.doi.org/10.1016/j.powtec.2016.04.006

3.3 X-ray Diffraction

X-ray diffraction data collected for the calcined aluminosilicate powders are presented in Figure 7. The X-ray diffractograms for samples A and B (empirical formulae $2SiO_2{\cdot}Al_2O_3$ and $4SiO_2{\cdot}Al_2O_3$, respectively) each display a broad featureless hump at about 20 – 25° 2θ, typical of amorphous aluminosilicates [30, 40, 41]. No crystalline phases are detected in samples A and B, indicating (in conjunction with the DTG data presented in Figure 4) that the calcination temperature of 550°C is sufficient to remove all organic material while preventing the crystallisation processes that may otherwise reduce the reactivity of the aluminosilicate powders.

The X-ray diffractograms of samples C, D, E and F (empirical formulae $0.800CaO{\cdot}SiO_2{\cdot}0.078Al_2O_3$, $1.214CaO{\cdot}SiO_2{\cdot}0.078Al_2O_3$, $0.709CaO{\cdot}SiO_2{\cdot}0.026Al_2O_3$ and $0.104CaO{\cdot}SiO_2{\cdot}0.026Al_2O_3$, respectively) display broad, featureless humps centred at approximately 29° 2θ, again indicating a predominantly amorphous material [30, 42]. Two polymorphs of Ca_2SiO_4 (β polymorph Powder Diffraction File (PDF) # 33-0302 and α'_L polymorph PDF # 36-0642)) are identified in the calcined powder for each of these samples, while small amounts of $Ca_3Al_2O_6$ (PDF # 33-0251) are identified in samples C and D and a small amount of free lime (CaO, PDF # 48-1467) is also identified in sample D. Small amounts of clinozoisite ($Ca_2Al_3(Si_2O_7)(SiO_4)O(OH)$, PDF # 44-1400), wollastonite ($CaSiO_3$, PDF # 42-0547) and pavlovskyite ($Ca_8Si_5O_{18}$,PDF # 29-0368) are present in samples E and F. Calcination of the precursor to 900°C is necessary to remove any calcium carbonate present in the sample (converting it to free lime), however it is evident from the X-ray diffractograms in Figure 7 that the calcination process has caused some devitrification of the amorphous material and subsequent formation of small amounts of these crystalline phases. Higher levels of aluminium (as found in sample C and D) result in formation of small amounts of C_3A, as well as the crystalline calcium silicate phases which are also found in samples E and F without the formation of C_3A.

The broad low intensity hump which appears at approximately 10-15° 2θ in the X-ray diffractograms of the calcium aluminosilicate precursors (samples C-F) results from subtraction of the sample holder background. This was done manually (using the diffractogram of an empty sample holder) in order to preserve any diffraction intensity from the amorphous content of the powders, however this introduces a small broad hump at lower angles due to differences in diffraction plane height between full and empty sample holders.

Postprint of a paper published in *Powder Technology*, 29(2016):17-33. Version of record is available at http://dx.doi.org/10.1016/j.powtec.2016.04.006

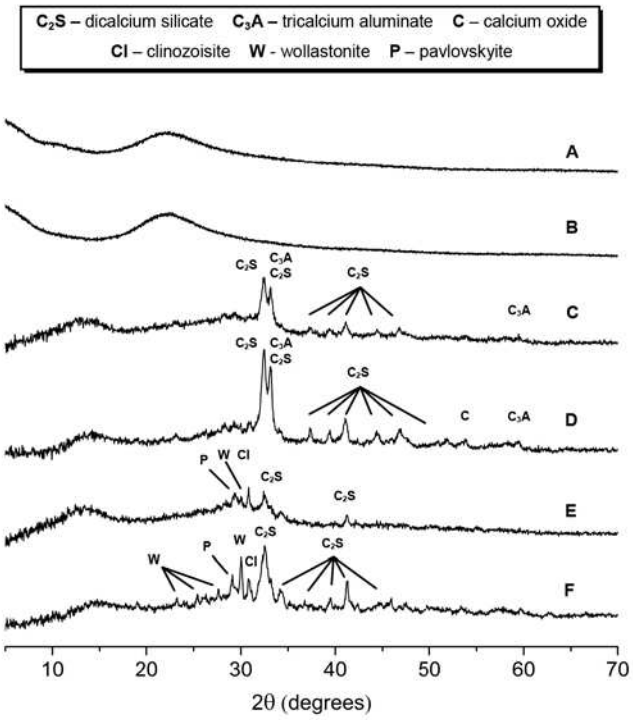

Figure 7: X-ray diffractograms of the calcined powders for each sample

3.4 Solid state magic angle spinning nuclear magnetic resonance

3.4.1 ^{27}Al MAS NMR

The ^{27}Al MAS NMR spectra for each of the calcined powders are presented in Figure 8. The spectra of samples A and B are typical of those commonly observed for aluminosilicate glasses, displaying three broad peaks exhibiting chemical shifts (δ_{obs}) of approximately 3, 31 and 57 ppm which are assigned to octahedral, pentahedral and tetrahedral aluminium, respectively [43-45]. Due to the broad nature of the peaks, none of the resonances can be assigned directly to a single well defined Al environment. The resonance assigned to octahedral Al is approximately twice the intensity of the tetrahedral and 5-coordinated Al resonances in the spectrum of sample A, while the spectrum of Sample B exhibits similar intensities for each resonance, with slightly more 5-coordinated Al and slightly less octahedrally coordinated Al than was observed for sample A. The resonance attributed to Al(IV) in both samples A and B ($\delta_{obs} \sim 57$ ppm) is within the region of q^4 environments (Al bonded to four Si atoms via oxygen bridges) in aluminosilicate solutions [46, 47], zeolites [48] and mullite [49]. Al(V) and Al(IV) are commonly observed in mullite-like structures in aluminosilicate glasses where charge balancing cations are not in excess [43], and as such any Al existing as Al(V) and Al(VI) in samples A and B is likely to provide some charge balancing to the negative charge associated with tetrahedral Al sites.

Postprint of a paper published in *Powder Technology*, 29(2016):17-33. Version of record is available at http://dx.doi.org/10.1016/j.powtec.2016.04.006

It should be noted that the resonance at 31 ppm, assigned here predominantly to Al(V), is also within the region in which resonances due to highly distorted Al(IV) within aluminium tetrahedra triclusters in mullite have been observed, which also exhibit a resonance at approximately 3 ppm due to Al(VI) [50]. The broad peak at approximately 3 ppm in the spectra of samples A and B suggests the presence of mullite-like structures within these samples [49], and consequently the peak at 31 ppm is likely due to a contribution of resonances from both Al(V) and highly-distorted Al(IV) species. The broad nature of the peak at 3 ppm suggests that the Al(VI) within these powders displays only short-range ordering, and is consistent with the lack of any identifiable crystalline phases in the X-ray diffractograms. The fact that the peak at 31 ppm has significantly less intensity in the spectrum of sample A than in sample B is indicative of a greater amount of mullite-like structures in sample A and is consistent with the fact that the composition of sample A ($2SiO_2{\cdot}Al_2O_3$) is much closer to mullite (between $2SiO_2{\cdot}3Al_2O_3$ and $SiO_2{\cdot}2Al_2O_3$) than sample B ($4SiO_2{\cdot}Al_2O_3$).

The ^{27}Al MAS NMR spectra of the calcined calcium-aluminosilicate powders (samples C, D, E and F) are very similar, all displaying a broad tetrahedral Al resonance centred at approximately 54 ppm with the exception of sample D, in which the tetrahedral Al resonance is centred at approximately 56 ppm. These resonances are assigned to disordered Al(IV) within q^4 environments within a highly polymerised aluminosilicate glass. The Al(IV) resonance of the calcium-aluminosilicate powders (samples C – F) is observed at a slightly lower frequency ($\Delta\delta_{obs} \approx 3$ ppm) than in the aluminosilicate powders (samples A and B). This difference in δ_{obs} is likely due to the fact that Al(IV) within the calcium-aluminosilicate powders will be charge balanced by Ca^{2+}, while in the aluminosilicate powders the Al(IV) exists in mostly mullite-like structures and is charge balanced by Al(VI). The breadth of this resonance indicates that there is a distribution of disordered Al(IV) environments rather than a single well defined site. This resonance is attributed to the glassy phase responsible for the broad amorphous hump in the X-ray diffractograms of these samples and is similar to that observed for granulated blast furnace slag [30, 42].

Each of the four calcined calcium-aluminosilicate powders displays a low intensity broad resonance centred at approximately 0 ppm, partly overlapping the upfield spinning side band of the main Al(IV) peak, attributed to octahedral Al. Al(VI) in C_3A has been observed in this chemical shift region [51], and the presence of this resonance is consistent with the small amount of C_3A identified in each of samples C and D. A small amount of Al(VI) within a glassy phase has also been observed in ground granulated blast furnace slag (GGBFS) [30], and given the absence of any peaks which can be attributed to C_3A within samples E and F in the XRD diffractograms, the broad peak at 0 ppm in the spectra of these samples containing reduced Al content is likely to be due to a similar Al(VI) environment. The

Postprint of a paper published in *Powder Technology*, 29(2016):17-33. Version of record is available at http://dx.doi.org/10.1016/j.powtec.2016.04.006

spectra of samples C, D, E and F do not contain any peaks within the regions assigned to Al(V) or highly-distorted Al(IV) in mullite-like structures in the spectra of samples A and B, consistent with the low Al concentrations in these powders.

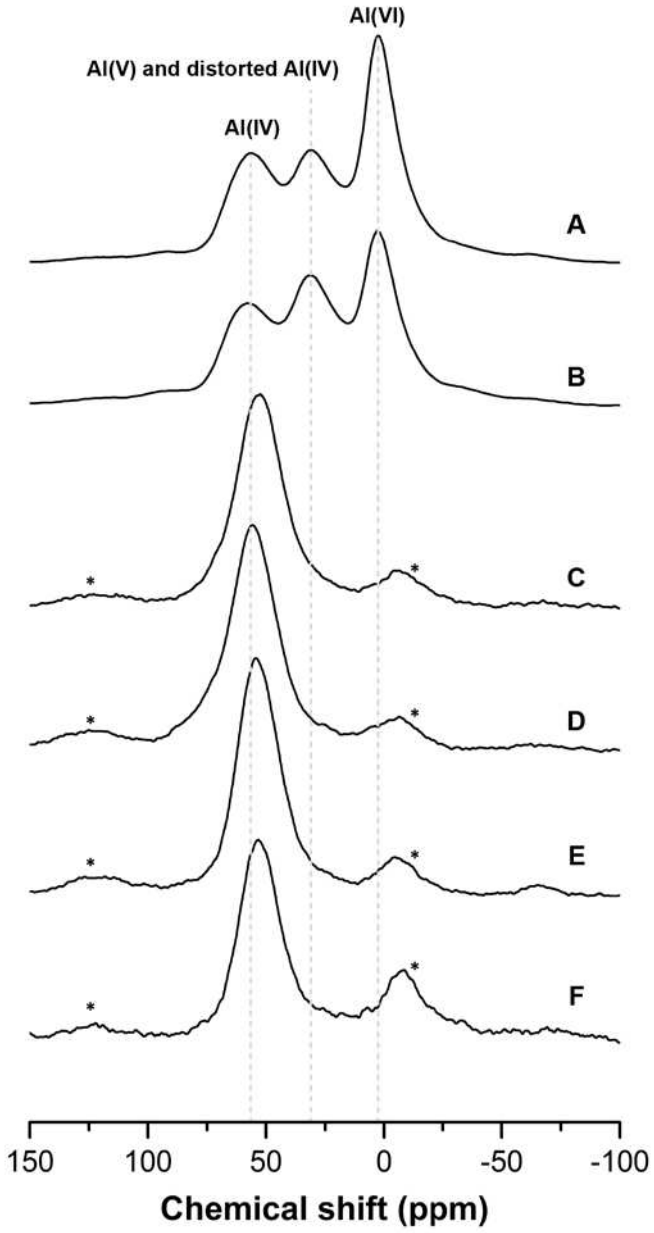

Figure 8: ^{27}Al MAS NMR spectra for each sample. Regions in which spinning sidebands contribute to the overall spectra are indicated by *

Postprint of a paper published in *Powder Technology*, 29(2016):17-33. Version of record is available at http://dx.doi.org/10.1016/j.powtec.2016.04.006

3.4.2 ^{29}Si MAS NMR

The ^{29}Si MAS NMR spectra of the calcined powders, along with the associated deconvolutions, are presented in Figure 9. The high intensity peak appearing in the spectra of the aluminosilicate powders (sample A and B) at -110.5 ppm can be attributed to Q^4(0Al) environments [44, 52]. Peaks of lower intensity at -85.4, -88.8, -96 and -101 ppm also contribute to the overall spectra. The ^{27}Al MAS NMR spectra for these samples indicate that a significant proportion of Al within the powders exists in a tetrahedral coordination and consequently it is unexpected that the ^{29}Si MAS NMR spectra for these samples indicates silicon exists so predominantly in a Q^4(0Al) environment. It is likely that during calcination these samples have undergone spinodal decomposition into a highly polymerised Si-rich phase and a phase containing mullite-like structures which, according to the literature, are expected to contribute resonances to the overall spectra at approximately -87, -90, -94 and -106 ppm [34, 53, 54]. The broad nature of the spectra presented here is similar to that observed for aluminosilicate powders synthesised via a sol-gel method [55].

The dependence of chemical shift on Al substitution within Q^4(mAl) environments has been widely reported [44, 56], and is commonly used for identification of Si environments within ^{29}Si MAS NMR spectra, however this implicitly assumes that these phases consist solely of Si(IV) – O – Al(IV) linkages. The presence of lower coordination Si species (Q^1, Q^2(*m*Al) or Q^3(*m*Al)) is uncommon in aluminosilicate glasses with no alkalis or alkali earths; these sites are generally present in over-charge-balanced silicates such as ground granulated blast furnace slag (GGBFS) [30, 42, 57], and as such these environments are not expected in samples A and B. It is likely that the apparently lower coordination Si species contributing to the ^{29}Si MAS NMR spectra of these samples are instead those which participate in Si(IV) – O - Al(V,VI) bonding. This will significantly alter the observed chemical shift of the Q^4(*m*Al) environments compared to the situation when all Al is tetrahedral [44] and consequently each peak within the -85 ppm to -105 ppm cannot be straightforwardly assigned to a single Si environment.

^{29}Si MAS NMR spectra for the calcined calcium-aluminosilicate powders (samples C, D, E and F) display a broad resonance centred at approximately -82 ppm. The spectrum of each sample can be deconvoluted into resonances at -78 ppm, -82.7 ppm, -88 ppm and -94 ppm, as well as smaller contributions to the overall spectra at -70.5 ppm, -74.5 ppm, -101.5 ppm and -110 ppm. Network modifying cations alter the chemical shifts exhibited by Q^n(*m*Al) species, particularly for more strongly polarising cations such as calcium [58, 59], which will cause additional overlapping of the individual Q^n(*m*Al) environments. The presence of Al(V) and Al(VI) species further complicates peak assignment in the ^{29}Si MAS NMR spectra, as discussed above. A small contribution to the overall spectra in the

Postprint of a paper published in *Powder Technology*, 29(2016):17-33. Version of record is available at http://dx.doi.org/10.1016/j.powtec.2016.04.006

region of Q^0 species (around -70 ppm) is also expected for each of samples C, D, E and F due to the presence of dicalcium silicate polymorphs as identified by XRD [60, 61], and the sorosilicate clinozoisite is expected to contribute to the overall ^{29}Si spectra of samples E and F in the Q^0 and Q^1 regions, around -70 to -77 ppm [52]. Wollastonite exhibits a resonance at approximately -88 ppm [62], and is therefore expected to contribute to the resonance observed within the Q^2 region of the ^{29}Si spectra of sample F.

The glassy phase present within the calcium-aluminosilicate powders is likely to contain a heterogeneous mixture of a depolymerised calcium silicate and a highly polymerised aluminosilicate with calcium to charge balance the tetrahedral Al, as observed in numerous multicomponent oxide glasses [63-65]. Aluminium in the highly polymerised aluminosilicate region of this glassy phase is likely to be largely in tetrahedral coordination, as identified by ^{27}Al MAS NMR, and the low aluminium content of these powders (Al/Si = 0.156 or 0.051) dictates that this region will contain Si/Al > 1. As such, the highly polymerised aluminosilicate region is expected to contain each of the $Q^4(m\text{Al})$ (m = 1 – 4) species while the depolymerised calcium silicate region is expected to contain Q^1, Q^2 and Q^3 silicate species. Due to the inherently overlapping chemical shifts of the 15 possible $Q^n(m\text{Al})$ species, it is expected that low-coordinated Si species without links to Al, and high-coordinated species connected to several Al atoms, will contribute resonances to the same regions of the ^{29}Si NMR spectra [44]. Consequently it is not possible to assign each peak to an individual Si environment at this time.

The increased calcium content of samples D and F (Ca/(Al+Si) = 1.214 and 1.104, respectively) seems to have promoted the formation of either lower coordinated Si environments or highly coordinated, highly aluminium substituted silicon environments. This is particularly evident from the significantly larger intensity in the region -78 to -88 ppm, compared to the region -94 to -110 ppm, in the spectra of each sample. Increased aluminium content in samples C and D (Al/Si = 0.156) when compared to sample E and F (Al/Si = 0.05) has also resulted in similar changes to the spectra. These observations are consistent with the formation of the heterogeneous mixture described above. During powder synthesis, increased calcium content will promote formation of a greater amount of the depolymerised calcium silicate phase (containing Q^1, Q^2 and Q^3 silicate species), while increased aluminium content will promote formation of a greater amount of the highly polymerised aluminosilicate phase (containing highly-coordinated highly-aluminium substituted silicate species). Consequently, an increase in intensity within the same region of the spectra is observed in both situations.

Postprint of a paper published in *Powder Technology*, 29(2016):17-33. Version of record is available at http://dx.doi.org/10.1016/j.powtec.2016.04.006

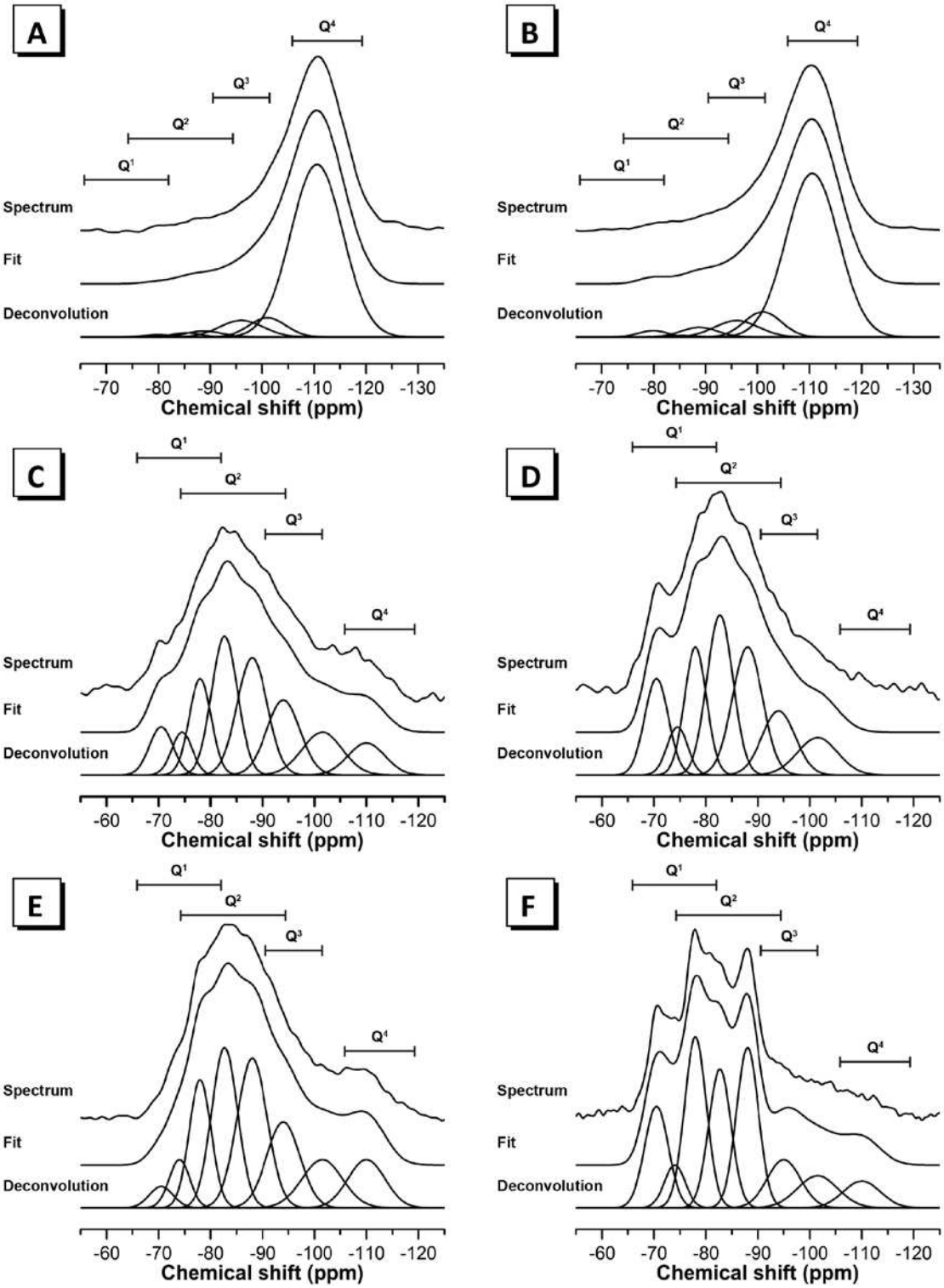

Figure 9: ^{29}Si MAS NMR spectra for each sample. For each plot the fit is the sum of the deconvoluted peaks. Regions where resonances due to each Q^n (n = 1, 2, 3, 4) species are expected are indicated. Each additional substitution of Al for Si in the Q^n sites is expected to shift the associated resonance approximately 5 ppm higher [44].

Postprint of a paper published in *Powder Technology*, 29(2016):17-33. Version of record is available at http://dx.doi.org/10.1016/j.powtec.2016.04.006

3.5 Transmission electron microscopy/energy dispersive X-ray spectroscopy

The chemistry of each ceramic powder as measured by TEM-EDX is presented in Figure 10. The chemistry of the aluminosilicate powders (samples A and B) is clustered around the stoichiometric design suggesting a significant degree of homogeneity in each case. The chemistry of sample A is clustered around two distinct regions, one which is Si-rich and another which is Al-rich and exhibits chemistry close to that of mullite, consistent with spinodal decomposition into a highly polymerised Si-rich phase and a phase containing mullite-like structures as discussed previously. The chemistry of sample B is clustered much more tightly around the stoichiometric design. The observations by ^{29}Si MAS NMR discussed above (section 3.4.2) suggest it is highly likely that spinodal decomposition into an Al-rich phase and a Si-rich phase has occurred during calcination of sample B, however the inability to observe two distinct compositional regions for this sample in Figure 10b suggests that any phase segregation has occurred on a sub-100nm scale.

The chemistry of the calcium-aluminosilicate powders (samples C, D, E and F) is clustered tightly around the designed Al/Si ratio but each sample displays a large range of values for the Ca/Si ratio. The composition of sample C is clustered around three distinct regions; a Ca-rich, Al-deficient region containing moderate amounts of Si (close to the composition of dicalcium silicate), a Ca-deficient aluminosilicate region, and a region exhibiting chemistry in between both of these extremes. In addition to solid state MAS NMR observations discussed above (section 3.4) the chemistry for this sample suggests the presence of a heterogeneous mixture of a depolymerised calcium silicate and a highly polymerised aluminosilicate phase. It is likely that the region exhibiting chemistry in between these two phases is not due to a distinct phase but actually a mixture of the two segregated on a sub-100 nm scale. Samples D, E and F do not display any clearly distinct separate regions of chemical composition. In each of these samples a wide range of values for the Ca/Si ratio is observed, the average of which is consistent with the stoichiometric design in each case. The low Al content and high Ca content of these samples (when compared to sample C) appears to have impeded the formation of the highly-polymerised aluminosilicate phase, resulting in a ceramic powders comprising predominantly of a calcium silicate phase, consistent with the Si coordination environments in these samples observed by ^{29}Si MAS NMR.

Postprint of a paper published in *Powder Technology*, 29(2016):17-33. Version of record is available at http://dx.doi.org/10.1016/j.powtec.2016.04.006

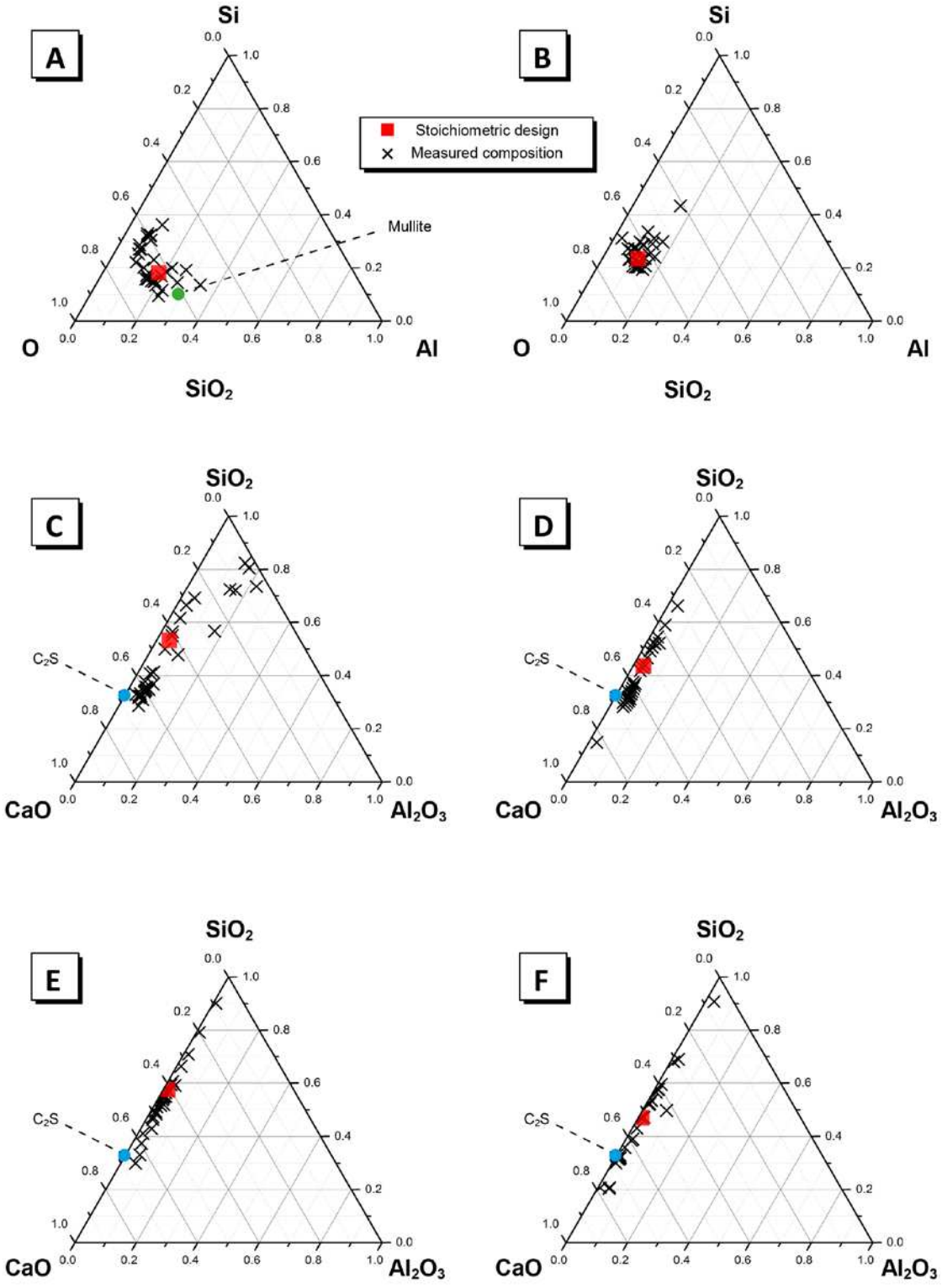

Figure 10: Projection of ceramic powder chemistry onto the ternary Al – Si – O system for samples A and B as marked and onto the CaO – Al_2O_3 – SiO_2 system for samples C, D, E and F as marked showing elemental composition as determined by TEM-EDX analysis.

Postprint of a paper published in *Powder Technology*, 29(2016):17-33. Version of record is available at http://dx.doi.org/10.1016/j.powtec.2016.04.006

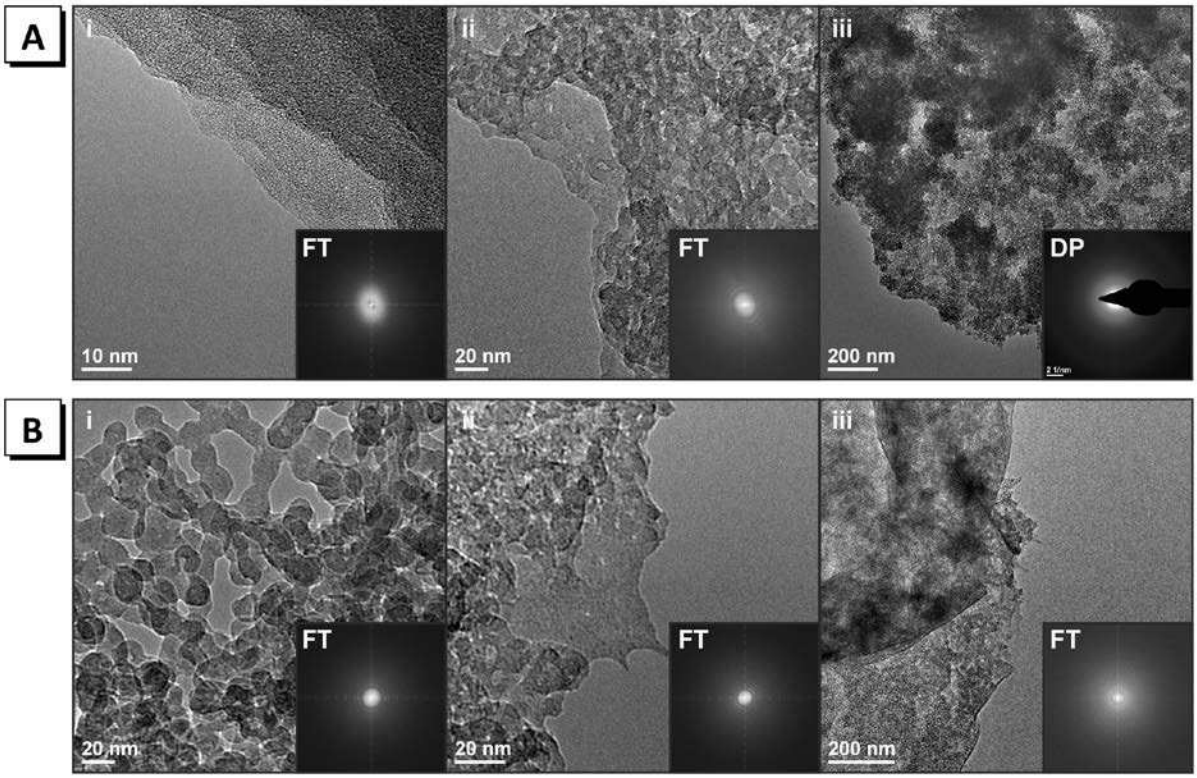

Figure 11: TEM bright-field images of samples A and B as marked. Different magnifications are indicated by i) – iv). Diffraction patterns (DP), Fourier transforms (FT) and associated regions within the relevant TEM bright-field image are indicated by numbers 1-4 for each sample, where applicable.

Bright-field TEM images for each of the ceramic powders, along with associated diffraction patterns and Fourier transforms are presented in Figure 11. Bright-field images of the aluminosilicate particles (samples A and B) exhibit a granular morphology, a high degree of homogeneity and a high porosity (consistent with observations by nitrogen gas adsorption). Diffraction patterns and Fourier transforms of the bright-field images for these samples indicate that they are amorphous, consistent with observations by X-ray diffraction. Diffraction patterns for different particles within the same aluminosilicate powder do not show any clearly observable differences on the scale examined here, suggesting that particles within these powders display a high degree of physical homogeneity.

Postprint of a paper published in *Powder Technology*, 29(2016):17-33. Version of record is available at http://dx.doi.org/10.1016/j.powtec.2016.04.006

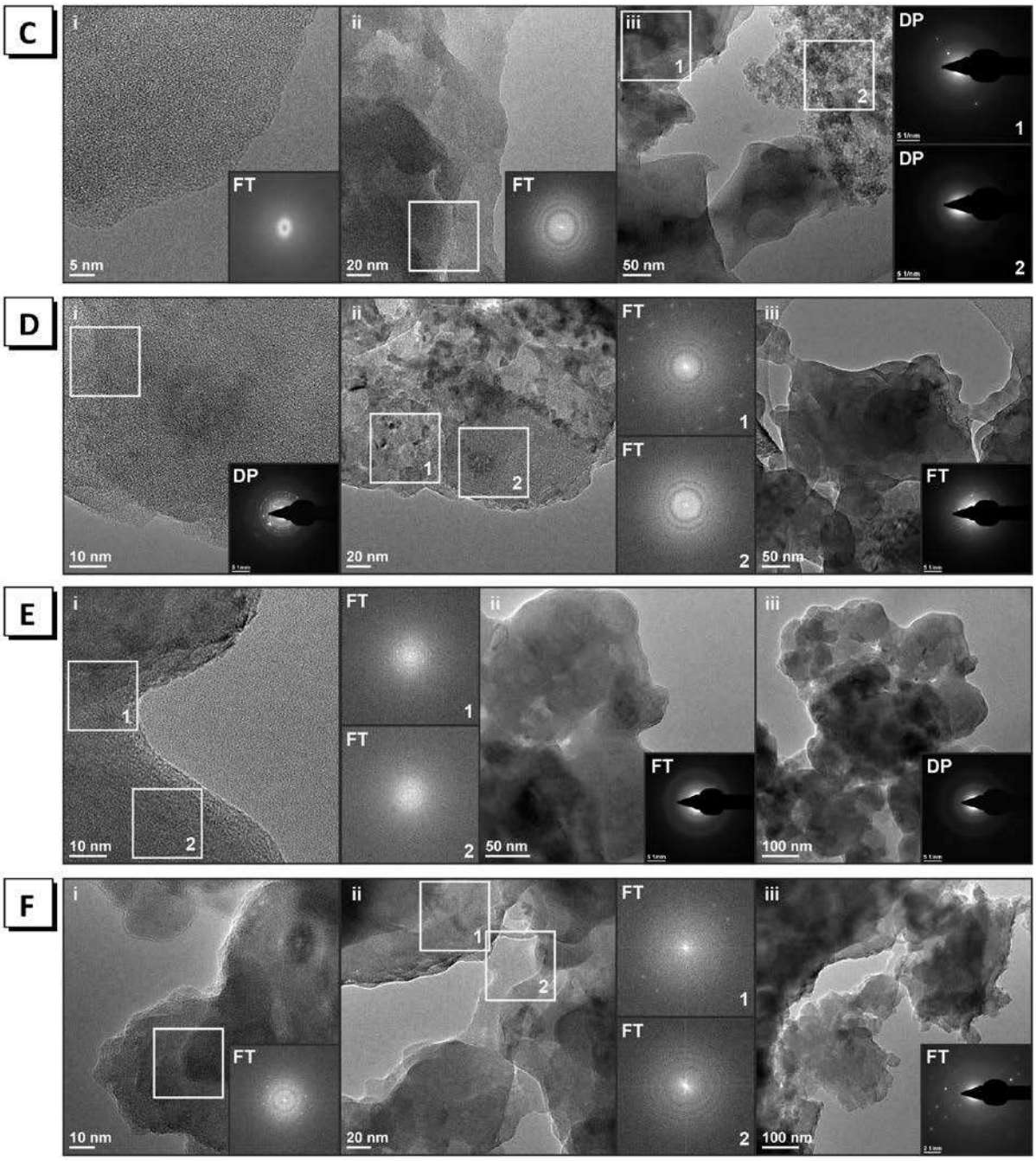

Figure 12: TEM bright-field images of samples C-F as marked. Different magnifications are indicated by i) – iv). Diffraction patterns (DP), Fourier transforms (FT) and associated regions within the relevant TEM bright-field image are indicated by numbers 1-4 for each sample, where applicable.

Bright-field images of the calcium-aluminosilicate particles (samples C - F) show that two distinct types of particle morphologies are present within these precursors; one which appears highly porous and granular and displays similarity with that of the aluminosilicate particles (indicated in Figure 12c-iii in the region marked 2), and another which appears much less porous and with a much smoother surface (indicated in Figure 12c-iii region 1). Diffraction patterns and Fourier transforms of these two

morphologies indicate that the first is amorphous, while the second displays varying degrees of crystallinity ranging from polycrystallinity to longer range crystallinity (Figure 12c-iii, d-iii, e-iii and f-iii). These two morphologies are consistent with the heterogeneous mixture observed by ^{29}Si MAS NMR. The degree of crystallinity is also observed to vary significantly within individual particles, ranging from amorphous to polycrystalline with no clearly defined transition region observable (Figure 12c-iii, d-ii, e-i, f-ii) suggesting that these powders display some degree of physical heterogeneity on the scale examined here. Regions displaying differing extents of crystallinity are observed to be as small as 10 nm^2 (Figure 12d-i and f-i). These observations are consistent with the XRD data for the calcium-aluminosilicate powders and suggest that the crystalline phases in these particles do not necessarily display long range order, but exhibit short range ordered nanocrystalline phases as well.

Comparing the bright-field images in Figure 12e-i and ii it can be seen that a region of the particle which appears homogeneous on a scale of 150 nm^2 actually contains nanocrystalline phases displaying short range order when examined on a scale of 15 nm^2. This indicates that nanocrystalline phases may also be present within the vitreous phase identified in the X-ray diffractograms for the calcium-aluminosilicate powders.

The results presented in this study indicate that the chemistry of the aqueous precursors and polymer carrier significantly influences the chemical and physical characteristics of the product obtained during synthesis of ceramic powders via an organic steric entrapment solution-polymerisation route. Controlling these parameters allows production of ceramic powders of specific stoichiometry and physical characteristics and provides a means to readily produce a large array of high-purity powders useful for many applications within inorganic chemistry and materials science fields. More specifically, these powders provide chemically simplified precursors for the production of model silicate gels exhibiting chemistry in key regions of the quaternary $CaO–Na_2O–Al_2O_3–SiO_2$ system, and constitute an important tool for the study of these materials.

Postprint of a paper published in *Powder Technology*, 29(2016):17-33. Version of record is available at http://dx.doi.org/10.1016/j.powtec.2016.04.006

4. Conclusions

Stoichiometrically controlled reactive aluminosilicate and calcium-aluminosilicate powders were successfully synthesised via an organic steric entrapment solution-polymerisation route. Polyethylene glycol was found to be superior to polyvinyl alcohol for the synthesis of calcium-aluminosilicate powders due to the increased oxygen content in the polymer backbone, which allows complete combustion of the polymer during calcination. Organics were successfully removed via calcination leaving powders that were predominantly X-ray amorphous and possessed a high surface area. Aluminosilicate powders exhibited a highly porous, granular morphology displaying a high degree of homogeneity and consisted predominantly of low Al-substituted tetrahedrally coordinated Si and roughly equal amounts of tetrahedral, pentahedral and octahedral Al in mullite-like structures. Calcium-aluminosilicate powders exhibited two distinct morphologies; one which is amorphous and exhibits a high degree of porosity and one which displays varying degrees of crystallinity and a low porosity. The amorphous, highly porous phase corresponds to a polymerised aluminosilicate region containing Al in a distorted tetrahedral environment and Si in a high-coordinated, high Al-substituted Si environments, with calcium in a charge balancing role, while partially crystalline phase displaying low porosity corresponds to a depolymerised calcium silicate region containing low-coordinated Si environments. The powders synthesised in this study possess a high purity and exhibit chemical and physical characteristics which are likely to be useful for the synthesis of model silicate gels exhibiting chemistry in key regions of the quaternary $CaO–Na_2O–Al_2O_3–SiO_2$ system. The refined organic steric entrapment solution-polymerisation method presented provides a fast, reproducible means for synthesising high-purity aluminosilicate and calcium-aluminosilicate ceramic powders which constitute an important tool for studying particle interactions within complex geopolymer systems.

Postprint of a paper published in *Powder Technology*, 29(2016):17-33. Version of record is available at http://dx.doi.org/10.1016/j.powtec.2016.04.006

5. Acknowledgements

This work has been funded in part by the Australian Research Council (ARC), including support through the Particulate Fluids Processing Centre, a Special Research Centre of the ARC. The University of Melbourne also provided support through an Overseas Research Experience Scholarship to support an extended visit by the first author to the University of Sheffield. We also wish to thank and acknowledge Professor Jon Woodhead, School of Earth Sciences, The University of Melbourne for assistance obtaining the X-ray fluorescence data; Dr Peng Zeng, Mercury Centre, The University of Sheffield and Dr Sergey Rubanov, Advanced Microscopy Facility, The University of Melbourne for assistance with transmission electron microscopy experiments; and Dr Oday H. Hussein, University of Sheffield, for assistance with the TG-MS experiments.

6. References

1. Pechini, M.P., Method of preparing lead and alkaline earth titanates and niobates and coating method using the same to form a capacitor. U.S. Patent No. 3 330 697, 1967
2. Gulgun, M.A., Nguyen, M.H., and Kriven, W.M., Polymerized organic–inorganic synthesis of mixed oxides. *Journal of the American Ceramic Society*, 1999. **82**(3): p. 556-60.
3. Kumar Saha, S., Pathak, A., and Pramanik, P., Low-temperature preparation of fine particles of mixed oxide systems. *Journal of Materials Science Letters*, 1995. **14**(1): p. 35-7.
4. Pramanik, P. and Pathak, A., A new chemical route for the preparation of fine ferrite powders. *Bulletin of Materials Science*, 1994. **17**(6): p. 967-75.
5. Lee, S.J., Benson, E.A., and Kriven, W.M., Preparation of Portland Cement Components by Poly(vinyl alcohol) Solution Polymerization. *Journal of the American Ceramic Society*, 1999. **82**(8): p. 2049-55.
6. Nguyen, M.H., Lee, S.J., and Kriven, W.M., Synthesis of oxide powders by way of a polymeric steric entrapment precursor route. *Journal of Materials Research*, 1999. **14**(8): p. 3417-26.
7. Lee, S.J. and Kriven, W.M., Crystallization and densification of nano-size amorphous cordierite powder prepared by a PVA solution polymerization route. *Journal of the American Ceramic Society*, 1998. **81**(10): p. 2605-12.
8. Duxson, P., The structure and thermal evolution of metakaolin geopolymers. PhD Thesis, 2006, The University of Melbourne.
9. Gordon, M., Bell, J.L., and Kriven, W.M., *Comparison of naturally and synthetically-derived, potassium based geopolymers*, in *Advances in Ceramic Matrix Composites X*. 2004, John Wiley & Sons, Inc, New York. p. 95-106.
10. Provis, J.L. and Bernal, S.A., Geopolymers and related alkali-activated materials. *Annual Review of Materials Research*, 2014. **44**(1): p. 299-327.
11. Provis, J.L. and van Deventer, J.S.J. (editors), *Alkali Activated Materials. State-of-the-Art Report, RILEM TC 224-AAM*. RILEM/Springer, Dordrecht.
12. Juenger, M.C.G., Winnefeld, F., Provis, J.L., and Ideker, J.H., Advances in alternative cementitious binders. *Cement and Concrete Research*, 2011. **41**(12): p. 1232-43.
13. Provis, J.L., Palomo, A., and Shi, C., Advances in understanding alkali-activated materials. *Cement and Concrete Research*, 2015. **78A**: p. 110-25.
14. Palacios, M., Houst, Y.F., Bowen, P., and Puertas, F., Adsorption of superplasticizer admixtures on alkali-activated slag pastes. *Cement and Concrete Research*, 2009. **39**(8): p. 670-7.

15. Provis, J.L., Duxson, P., and van Deventer, J.S.J., The role of particle technology in developing sustainable construction materials. *Advanced Powder Technology*, 2010. **21**(1): p. 2-7.
16. Kashani, A., San Nicolas, R., Qiao, G.G., van Deventer, J.S.J., and Provis, J.L., Modelling the yield stress of ternary cement–slag–fly ash pastes based on particle size distribution. *Powder Technology*, 2014. **266**(0): p. 203-9.
17. Bakharev, T., Sanjayan, J.G., and Cheng, Y.B., Resistance of alkali-activated slag concrete to alkali–aggregate reaction. *Cement and Concrete Research*, 2001. **31**(2): p. 331-4.
18. Shi, C., Shi, Z., Hu, X., Zhao, R., and Chong, L., A review on alkali-aggregate reactions in alkali-activated mortars/concretes made with alkali-reactive aggregates. *Materials and Structures*, 2015. **48**(3): p. 621-8.
19. Duxson, P. and Provis, J.L., Designing precursors for geopolymer cements. *Journal of the American Ceramic Society*, 2008. **91**(12): p. 3864-9.
20. Myers, R.J., Bernal, S.A., San Nicolas, R., and Provis, J.L., Generalized structural description of calcium-sodium aluminosilicate hydrate gels: the cross-linked substituted tobermorite model. *Langmuir*, 2013. **29**(17): p. 5294-306.
21. Scrivener, K.L. and Nonat, A., Hydration of cementitious materials, present and future. *Cement and Concrete Research*, 2011. **41**(7): p. 651-65.
22. Brunauer, S., Emmett, P.H., and Teller, E., Adsorption of gases in multimolecular layers. *Journal of the American Chemical Society*, 1938. **60**(2): p. 309-19.
23. Barrett, E., Joyner, L., and Halenda, P., The determination of pore volume and area distributions in porous substances. I. Computations from nitrogen isotherms. *Journal of the American Chemical Society*, 1951. **73**(1): p. 373-80.
24. Horvath, G. and Kawazoe, K., Method for the calculation of effective pore size distribution in molecular sieve carbon. *Journal of Chemical Engineering of Japan*, 1983. **16**(6): p. 470-5.
25. Saito, A. and Foley, H.C., Curvature and parametric sensitivity in models for adsorption in micropores. *AIChE Journal*, 1991. **37**(3): p. 429-36.
26. Jewell, R.B. and Rathbone, R.F., Optical properties of coal combustion yproducts for particle-size analysis by laser diffraction. *Coal Combustion and Gasification Products*, 2009. **1**: p. 1-7.
27. Osborn, E.F., Devries, R.C., Gee, K.H., and Kraner, H.M., Optimum composition of blast furnace slag as deduced from liquidus data for the quaternary system CaO-MgO-Al_2O_3-SiO_2. *Transactions of the American Institute of Mining and Metallurgical Engineers*, 1954. **200**(1): p. 33-45.
28. Delaglio, F., Grzesiek, S., Vuister, G., Zhu, G., Pfeifer, J., and Bax, A., NMRPipe: A multidimensional spectral processing system based on UNIX pipes. *Journal of Biomolecular NMR*, 1995. **6**(3): p. 277-93.
29. Massiot, D., Fayon, F., Capron, M., King, I., Le Calvé, S., Alonso, B., Durand, J.-O., Bujoli, B., Gan, Z., and Hoatson, G., Modelling one- and two-dimensional solid-state NMR spectra. *Magnetic Resonance in Chemistry*, 2002. **40**(1): p. 70-6.
30. Bernal, S.A., Provis, J.L., Walkley, B., San Nicolas, R., Gehman, J.D., Brice, D.G., Kilcullen, A.R., Duxson, P., and van Deventer, J.S.J., Gel nanostructure in alkali-activated binders based on slag and fly ash, and effects of accelerated carbonation. *Cement and Concrete Research*, 2013. **53**: p. 127-44.
31. Provis, J.L., Duxson, P., Lukey, G.C., and van Deventer, J.S.J., Statistical thermodynamic model for Si/Al ordering in amorphous aluminosilicates. *Chemistry of Materials*, 2005. **17**(11): p. 2976-86.
32. Schure, M., Soltys, P.A., Natusch, D.F.S., and Mauney, T., Surface area and porosity of coal fly ash. *Environmental Science & Technology*, 1985. **19**(1): p. 82-6.
33. Escalante-García, J.I., Campos-Venegas, K., Gorokhovsky, A., and Fernández, A., Cementitious composites of pulverised fuel ash and blast furnace slag activated by sodium silicate: effect of Na_2O concentration and modulus. *Advances in Applied Ceramics*, 2006. **105**(4): p. 201-8.

34. Provis, J.L. and van Deventer, J.S.J. (editors), *Geopolymers - Structure, Processing, Properties and Industrial Applications*. 2009, Woodhead Publishing, Cambridge, UK.
35. Arvaniti, E.C., Juenger, M.C.G., Bernal, S.A., Duchesne, J., Courard, L., Leroy, S., Provis, J.L., Klemm, A., and De Belie, N., Determination of particle size, surface area, and shape of supplementary cementitious materials by different techniques, *Materials and Structures*, 2015. **48**(11): p. 3687-701
36. Kim, S.J., Park, S.J., Kim, I.Y., Lee, Y.H, and Kim, S.I., Thermal characteristics of poly(vinyl alcohol) and poly(vinylpyrrolidone) IPNs. *Journal of Applied Polymer Science*, 2002. **86**(8): p. 1844-7.
37. Bernal, S.A., Rodriguez, E.D., Mejía de Gutierrez, R., Gordillo, M., and Provis, J.L., Mechanical and thermal characterisation of geopolymers based on silicate-activated metakaolin/slag blends. *Journal of Materials Science*, 2011. **46**(16): p. 5477-86.
38. Lattimer, R.P., Mass spectral analysis of low-temperature pyrolysis products from poly(ethylene glycol). *Journal of Analytical and Applied Pyrolysis*, 2000. **56**(1): p. 61-78.
39. Voorhees, K.J., Baugh, S.F., and Stevenson, D.N., An investigation of the thermal degradation of poly(ethylene glycol). *Journal of Analytical and Applied Pyrolysis*, 1994. **30**(1): p. 47-57.
40. Duxson, P., Fernández-Jiménez, A., Provis, J.L., Lukey, G.C., Palomo, A., and van Deventer, J.S.J., Geopolymer technology: the current state of the art. *Journal of Materials Science*, 2007. **42**(9): p. 2917-33.
41. Bernal, S., San Nicolas, R., Provis, J., Mejía de Gutiérrez, R., and van Deventer, J.J., Natural carbonation of aged alkali-activated slag concretes. *Materials and Structures*, 2014. **47**(4): p. 693-707.
42. Bernal, S.A., San Nicolas, R., Myers, R.J., Mejía de Gutiérrez, R., Puertas, F., van Deventer, J.S.J., and Provis, J.L., MgO content of slag controls phase evolution and structural changes induced by accelerated carbonation in alkali-activated binders. *Cement and Concrete Research*, 2014. **57**: p. 33-43.
43. Stebbins, J.F., Kroeker, S., Lee, S.K., and Kiczenski, T.J., Quantification of five- and six-coordinated aluminum ions in aluminosilicate and fluoride-containing glasses by high-field, high-resolution ^{27}Al NMR. *Journal of Non-Crystalline Solids*, 2000. **275**(1–2): p. 1-6.
44. Engelhardt, G. and Michel, D., *High-resolution solid state NMR of silicates and zeolites*. 1987, Chichester: Wiley.
45. Kelsey, K.E., Stebbins, J.F., Mosenfelder, J.L., and Asimow, P.D., Simultaneous aluminum, silicon, and sodium coordination changes in 6 GPa sodium aluminosilicate glasses. *American Mineralogist*, 2009. **94**(8-9): p. 1205-15.
46. Samadi-Maybodi, A., Azizi, S.N., Naderi-Manesh, H., Bijanzadeh, H., McKeag, I.H., and Harris, R.K., Highly resolved ^{27}Al NMR spectra of aluminosilicate solutions. *Journal of the Chemical Society, Dalton Transactions*, 2001. (5): p. 633-8.
47. Harris, R.K., Samadi-Maybodi, A., and Smith, W., The incorporation of aluminium into silicate ions in alkaline aqueous solution studied by ^{27}Al NMR. *Zeolites*, 1997. **19**: p. 147-55.
48. Lippmaa, E., Samoson, A., and M. Mägi, High-resolution ^{27}Al NMR of aluminosilicates. *Journal of the American Chemical Society*, 1986. **108**(8): p. 1730-5.
49. Jaymes, I., Douy, A., Florian, P., Massiot, D., and Coutures, J.P., New synthesis of mullite. Structural evolution study by ^{17}O, ^{27}Al and ^{29}Si MAS NMR spectroscopy. *Journal of Sol-Gel Science and Technology*, 1994. **2**(1-3): p. 367-70.
50. Merwin, L.H., Sebald, A., Rager, H., and Schneider, H., ^{29}Si and ^{27}Al MAS NMR spectroscopy of mullite. *Physics and Chemistry of Minerals*, 1991. **18**(1): p. 47-52.
51. Pena, P., Rivas Mercury, J.M., de Aza, A.H., Turrillas, X., Sobrados, I., and Sanz, J., Solid-state ^{27}Al and ^{29}Si NMR characterization of hydrates formed in calcium aluminate–silica fume mixtures. *Journal of Solid State Chemistry*, 2008. **181**(8): p. 1744-52.
52. Mackenzie, K.J.D. and Smith, M.E., *Multinuclear Solid-state Nuclear Magnetic Resonance of Inorganic Materials*, ed. R.W. Cahn. 2002, Oxford: Pergamon, Elsevier Science Ltd.

53. Risbud, S.H. and Pask, J.A., Calculated thermodynamic data and metastable immiscibility in the system SiO_2-Al_2O_3. *Journal of the American Ceramic Society*, 1977. **60**(9-10): p. 418-24.
54. He, H., Guo, J., Zhu, J., Yuan, P., and Hu, C., ^{29}Si and ^{27}Al MAS NMR spectra of mullites from different kaolinites. *Spectrochimica Acta Part A: Molecular and Biomolecular Spectroscopy*, 2004. **60**(5): p. 1061-4.
55. Cui, X.-m., Liu, L.-p., Zheng, G.-j., Wang, R.-p., and Lu, J.-p., Characterization of chemosynthetic Al_2O_3–$2SiO_2$ geopolymers. *Journal of Non-Crystalline Solids*, 2010. **356**(2): p. 72-6.
56. Duxson, P., Provis, J.L., Lukey, G.C., Separovic, F., and Deventer, J.S.J.v., ^{29}Si NMR study of structural ordering in aluminosilicate geopolymer gels. *Langmuir*, 2005. **21**: p. 3028-36.
57. Le Saoût, G., Ben Haha, M., Winnefeld, F., Lothenbach, B., and Jantzen, C., Hydration degree of alkali-activated slags: A ^{29}Si NMR study. *Journal of the American Ceramic Society*, 2011. **94**(12): p. 4541-7.
58. Moesgaard, M., Keding, R., Skibsted, J., and Yue, Y., Evidence of intermediate-range order heterogeneity in calcium aluminosilicate glasses. *Chemistry of Materials*, 2010. **22**(15): p. 4471-83.
59. Murdoch, J.B., Stebbins, J.F., and Carmichael, I.S.E., High-resolution ^{29}Si NMR study of silicate and aluminosilicate glasses: the effect of network-modifying cations. *American Mineralogist*, 1985. **70**: p. 370-82.
60. Alonso, C. and Fernandez, L., Dehydration and rehydration processes of cement paste exposed to high temperature environments. *Journal of Materials Science*, 2004. **39**(9): p. 3015-24.
61. Hjorth, J., Skibsted, J., and Jakobsen, H.J., ^{29}Si MAS NMR studies of portland cement components and effects of microsilica on the hydration reaction. *Cement and Concrete Research*, 1988. **18**(5): p. 789-98.
62. Hansen, M.R., Jakobsen, H.J., and Skibsted, J., ^{29}Si chemical shift anisotropies in calcium silicates from high-field ^{29}Si MAS NMR spectroscopy. *Inorganic Chemistry*, 2003. **42**(7): p. 2368-77.
63. Champagnon, B., Wondraczek, L., and Deschamps, T., Boson peak, structural inhomogeneity, light scattering and transparency of silicate glasses. *Journal of Non-Crystalline Solids*, 2009. **355**(10–12): p. 712-4.
64. Martinez, V., Jurdyc, A.M., Vouagner, D., Martinet, C., and Champagnon, B., Density and concentration fluctuations in a erbium-doped fiber amplifiers glass: Raman and small angle X-ray scattering study. *Journal of Non-Crystalline Solids*, 2005. **351**(30–32): p. 2421-4.
65. Conradt, R., Chemical structure, medium range order, and crystalline reference state of multicomponent oxide liquids and glasses. *Journal of Non-Crystalline Solids*, 2004. **345**: p. 16-23.